ACS OMEGA

http://pubs.acs.org/journal/acsodf

Article

Metal-Impregnated Petroleum Coke-Derived Activated Carbon for the Adsorption of Arsenic in Acidic Waters

Kyle S. Fisher and Andrew J. Vreugdenhil*

Cite This: *ACS Omega* 2023, 8, 29083−29100

Read Online

ACCESS | Metrics & More | Article Recommendations

ABSTRACT: The efficacy of metal-impregnated petroleum coke (PC) activated carbon for the adsorption of arsenite and arsenate in acidic waters is investigated in this study. Unmodified PC activated carbon, $FeCl_3$-loaded activated carbon, $KMnO_4$-loaded activated carbon, and a mixed $FeCl_3$−$KMnO_4$-loaded activated carbon were used for evaluation. The surface characteristics of the activated carbons before and after arsenic adsorption were analyzed by X-ray photoelectron spectroscopy (XPS). Arsenate adsorption was significantly improved by the addition of an iron−manganese-loaded activated carbon, increasing adsorption from 8.12 to 50.93%. Oxidation−reduction reactions are proposed based on the observed arsenic $2p_{3/2}$, iron $2p_{3/2}$, and manganese $2p_{3/2}$ XPS peaks. While iron in the iron-loaded activated carbon is not acting as the reducing agent, it is acting as a conductor for the flow of electrons from the activated carbon to the arsenic for reduction to take place prior to the physisorption of the arsenic. In the manganese-loaded activated carbon, manganese acts as the reducing agent for arsenic prior to arsenic adsorption to the surface through physisorption. XPS of the post-arsenic(V) exposure samples showed that the Fe_2O_3 species were reduced from 32.18 to 1.66% in the FeMn-loaded sample, while the FeOOH species were increased from 53.16 to 81.71%. Similarly, MnO in the FeMn-loaded activated carbon dropped from 26.82 to 15.40%, while MnOOH and MnO_2 increased from 39.98 and 33.20 to 43.96 and 40.64%, respectively. This is consistent with the proposed mechanism. The adsorption of arsenite was also evaluated to show that the modification of the activated carbon adsorbed not only the arsenic(V) species but also the more toxic arsenic(III) species without the need for oxidation of the arsenic prior to adsorption.

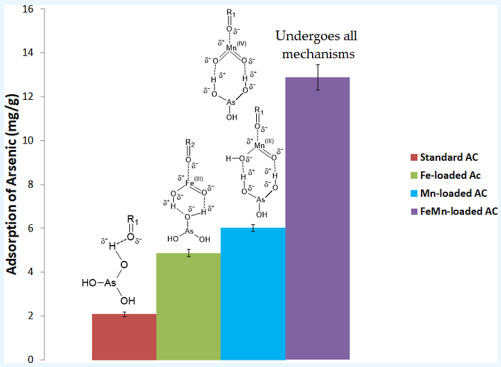

1. INTRODUCTION

As one of the twentieth most abundant elements in the Earth's crust, arsenic can be found in no fewer than 245 mineral species. The most common of these minerals is arsenopyrite, a mineral often found alongside high deposits of gold and, when oxidized, produces arsenic and sulfur oxiacids (e.g., H_3AsO_3, H_3AsO_4, H_2SO_4).[1−3] During the mining processes, arsenic is released into the acid mine drainage when sulfide-bearing materials are exposed to atmospheric water and oxygen. The Society for Mining, Metallurgy, and Exploration (SME) notes that mining activities, especially sulfide mining, increase the rate of arsenic released from minerals that are exposed to weathering during the excavation process.[4] In Canada, the Giant Mine, located in Yellowknife, NT, produced 237,000 tons of arsenic trioxide dust in its 52 year operation. Seepage from the chambers containing this arsenic trioxide is evident as concentrations of arsenic in some mine waters exceed 4000 ppm.[3] Treating these tailings is an important step in mitigating the chances of seepage or tailings spills that would result in elevated levels of arsenic in nearby groundwater and drinking water supplies.

Arsenic contamination in water supplies is already a widespread problem in a number of countries worldwide. Globally, over 140 million people across 50 countries have drinking water containing more than the World Health Organization's (WHO's) acceptable arsenic concentration level of 10 μg/L. The majority of arsenic concentrations can be found in South Asian countries such as Bangladesh, Cambodia, and India; however, several Latin American countries, including Argentina, Bolivia, and Mexico, have been identified to contain waters with arsenic concentrations above 50 μg/L.[5,6] In Bangladesh alone, the WHO reported 19 million people exposed to arsenic concentrations above the national standard of 50 μg/L and 39 million people exposed to arsenic concentrations above the WHO's guideline of 10 μg/L.[5]

Although there are many methods for the removal of metal ions from different matrices, such as ion exchange, coagulation, flocculation, nanofiltration, and chemical precipitation, adsorption has become the preferred method due to its simplicity, cost-

Received: March 28, 2023
Accepted: July 18, 2023
Published: July 31, 2023

Table 1. Pore Size Distribution Information Obtained from Nitrogen Adsorption Measurements

activated carbon material	BET surface area (m^2/g)	total pore volume (cm^3/g)	micropore percentage	average pore width (nm)
commercial AC	1329 ± 38	0.5011 ± 0.0440	53.3 ± 2.7	4.82 ± 0.11
standard AC	975 ± 19	0.4143 ± 0.0086	76.7 ± 0.44	3.60 ± 0.035
Fe-loaded AC	748 ± 13	0.3349 ± 0.0098	67.4 ± 0.55	3.95 ± 0.056
Mn-loaded AC	487 ± 15	0.2494 ± 0.0142	58.9 ± 0.75	6.35 ± 0.13
FeMn-loaded AC	397 ± 11	0.3479 ± 0.0190	31.1 ± 1.1	9.60 ± 0.21

effectiveness, and versatility.[7,8] Many studies in the literature have already shown the possibility of using adsorbent materials for the removal of arsenic in contaminated waters. A study by Byambaa et al. showed high adsorption capacities using an adsorbent derived from acid mine drainage sludge. The maximum adsorption capacity found in this study was 50.38 mg/g, compared to 29.07 mg/g that was obtained when using a commercially available granular ferric hydroxide adsorbent.[9] Another study by Singh et al. used a graphene oxide functionalized with a zirconium-based metal−organic framework nanocomposite for the removal of arsenic and, through isotherm modeling, obtained a maximum adsorption capacity of nearly 150 mg/g.[10] Studies in the literature investigate the adsorption of arsenic using many types of adsorbents; some include modified saxaul ash, magnetite nanoparticles, functionalized diatom silica shells, and activated carbons.[11−14]

In the literature, petroleum coke (PC) (or petcoke) has been proven to be an effective adsorbent for trace metals. A study by Pourrezaei et al. uses zero-valent iron-enhanced PC to adsorb vanadium, manganese, nickel, and molybdenum in oil sands process water.[15] Another study by Karimi et al. uses activated carbon prepared by CO_2 activation from a PC feedstock to adsorb metallic ions from oil sands tailings water. Their study provided adsorption data using their material on metals such as calcium, magnesium, strontium, sodium, and potassium; however, it did not provide data on arsenic adsorption.[16] To our knowledge, little work has been done on the adsorption of arsenic using PC-derived activated carbons.[17] PC has been chosen as the feedstock of choice in this study for two main reasons. PC is a waste byproduct of the bitumen extraction process from oil sands ore. As of 2011, the oil sands in Alberta produced nearly 10 million metric tons of PC per year. The coal industry and other industries have a total consumption of 5 million metric tons of petcoke per year. The remaining petcoke is stockpiled in large quantities and, at the end of 2011, Alberta contained stockpiles of petcoke weighing nearly 72 million metric tons.[18] Therefore, the first reason this study focuses on the use of a PC feedstock is due to the sheer abundance of the feedstock material allowing for the opportunity to use the waste petcoke as feedstock for a more valuable product. The second reason that petcoke was chosen as the feedstock material is due to its naturally high carbon content. Activated carbons can be made from any raw material that has a high carbon content or that can be processed to contain a high carbon content. Feedstocks include sawdust, wood chips, charcoal, coconut shell, tar, and grass ash.[19] These feedstocks can vary significantly in the initial carbon content they contain. Sawdust contains approximately 60% carbon, wood chips contain between 45 and 50% carbon, and charcoal contains 68−82% carbon.[20−22] These feedstocks often need elaborate preparation methods before the activation process because of their lower carbon content. This is not required for the use of PC as a feedstock because of its naturally high carbon content of between 90 and 97%.[23] This means that there is little cost associated and resources dedicated to the preparation of the raw material before activation.

This study will therefore focus on the use of PC-derived activated carbon and the modification of the activated carbon surface for the removal of arsenic(III) and arsenic(V) from acidic waters. This work describes the novel development of a highly effective adsorbent derived from the oil sands waste product, PC, its application in environmental remediation of arsenic species, and specifically, the mechanisms by which arsenic adsorption occurs on the modified activated carbon surface.

2. MATERIALS AND METHODS

PC used in this study was sourced from an oil sands company and, when activated, was compared to a commercially available activated carbon for an external benchmark (Strem Chemicals). Arsenic(V) pentoxide (Sigma-Aldrich) and arsenic(III) trioxide (Alfa Aesar) were used to make arsenic(V) and arsenic(III) stock solutions for all arsenic solutions.

2.1. Activation of PC. As previously described by Fisher and Vreugdenhil[24] and by Strong et al.,[25] PC was ground to pass 0.58 mm mesh, heated in air at 400 °C for 1 h, and allowed to cool. The resulting PC was mixed with an intentionally low amount of solid KOH [a 1:1 ratio (w/w)] and heated under flowing nitrogen from room temperature to 900 °C over 8 min. It was held at this temperature for 5 min and then allowed to cool under a nitrogen atmosphere to ambient temperature. The resulting activated carbon was ground with a mortar and pestle and washed with 10 mL of deionized water for every 1 g of initial feedstock at 80 °C for 1 h with stirring at 200 rpm. The product was vacuum-filtered and rinsed with 10 mL of 0.1 M HCl for every 1 g of initial feedstock and dried at 110 °C overnight. The activation process produces approximately 64 g of activated carbon for every 100 g of PC originally used.

To remove sulfur contamination in the wash water produced by the rinsing of the PC activated carbon, calcium hydroxide is used to precipitate calcium sulfates and regenerate KOH. Parallel studies are currently investigating the efficacy of recycled KOH for the activation of the PC to ensure that the product being produced is cost-effective for scalability.

2.2. Post-activation Functionalizations. *2.2.1. Iron (Fe) Loading.* A 100 mL 0.15 M iron chloride ($FeCl_3$) solution was prepared, and 5 g of PC AC was added to the solution. The pH of the solution was brought to 2.8 by the addition of 1 M HCl, and the solution was stirred for 30 min. After stirring, the solution was sonicated for 30 min and vacuum filtered. 2 L of deionized water was used to wash the product, and the product was dried at 110 °C. Once dried, the product was treated at 400 °C for 2 h under nitrogen. This heat-treated product was then washed with 2 L of deionized water and dried at 110 °C to obtain the Fe-Loaded AC.

2.2.2. Manganese (Mn) Loading. The above iron loading method (Section 2.2.1) was also used for the manganese

https://doi.org/10.1021/acsomega.3c02078
ACS Omega 2023, 8, 29083−29100

loading. A solution of 0.15 M potassium permanganate ($KMnO_4$) was used in place of the 0.15 M $FeCl_3$ solution.

2.2.3. Iron and Manganese (Fe–Mn) Loading. The above iron loading method (Section 2.2.1) was also used for the mixed iron and manganese loading. In place of the 0.15 M $FeCl_3$ solution, a mixed solution containing both 0.15 M $FeCl_3$ and 0.15 M $KMnO_4$ was used.

2.3. Microwave Plasma Atomic Emission Spectrometry Analysis. Arsenic(V) and arsenic(III) calibration standards of 1, 2, 5, 10, 25, 50, and 100 ppm were prepared in deionized water to construct calibration curves for microwave plasma atomic emission spectrometry (MP-AES) analysis. Calibration curves were created each new time the instrument was used under an acceptable tolerance of 10% calibration error and linearity (R^2) above 0.9900. All standards and samples were run in triplicate, with arsenic emission detected at a wavelength of 188.979 nm. Appendix A, Table A1 contains MP-AES operating parameters used for this study.

Table 2. Arsenic(V) Adsorption Capacity Comparisons Normalized to Surface Area

activated carbon material	adsorption of As(V) normalized to 1000 m^2 (mg/m^2)
commercial AC	6.37 ± 0.46
standard AC	2.13 ± 0.10
Fe-loaded AC	6.50 ± 0.12
Mn-loaded AC	12.36 ± 0.08
FeMn-loaded AC	32.43 ± 0.23

Table 3. Arsenic(V) Adsorption Capacities Comparison Normalized to Microporosity

activated carbon material	adsorption capacity normalized to 1 cm^3 micropores (mg cm^3)
commercial AC	9.00 ± 0.64
standard AC	3.84 ± 0.15
Fe-loaded AC	9.78 ± 0.25
Mn-loaded AC	14.21 ± 0.27
FeMn-loaded AC	11.51 ± 1.86

2.4. Surface Characterization of Activated Carbons. *2.4.1. Nitrogen Adsorption Measurements.* Measurement of the specific surface area of the carbon samples was carried out using gas phase nitrogen adsorption measurements on a Tristar II Plus (Micromeritics, Ottawa, Ontario, Canada). The samples were analyzed using N_2 adsorption at 77 K, with 50 points monitoring adsorption between 0.0065 p/p^0 and 0.995 p/p^0 and 52 points desorption between 0.995 p/p^0 and 0.104 p/p^0. All surface areas were reported using Brunauer–Emmett–Teller (BET) surface area analysis with pore size distributions developed using DFT with slit geometry modeling 2D-NLDFT with N_2 carbon finite pores.

2.4.2. X-ray Photoelectron Spectroscopy. X-ray photoelectron spectroscopy (XPS) was carried out using a Kratos AXIS Supra spectrometer to determine surface characteristics. A monochromatic Al Kα source (15 mA, 15 kV) was used with the instrument work function calibrated to give a binding energy (BE) of 83.96 eV for the Au $4f_{7/2}$ line for metallic gold. The spectrometer dispersion was adjusted to give a BE of 932.62 eV for the Cu $2p_{3/2}$ line of metallic copper. The Kratos charge neutralizer system was used on all specimens, and survey scan analyses were carried out with an analysis area of 300 × 700 μm with a pass energy of 160 eV. A pass energy of 20 eV with an analysis area of 300 × 700 μm was carried out for high-resolution analyses. Fitting of peaks was carried out using CASA XPS (version 2.31), with the XPS spectra being corrected to the main line of the carbon 1s spectrum at 284.8 eV.

2.5. Arsenic(V) Study. A 1000 ppm stock solution of arsenic(V) was prepared in deionized water using arsenic pentoxide (As_2O_5). All samples and standards were prepared by serial dilution from the 1000 ppm stock solution. Samples were prepared to a concentration of 50 ppm arsenic(V) with a final volume of 50 mL using deionized water to dilute the samples. 1 M HCl was used to bring the pH of the samples to 3.0.

2.5.1. Efficacy Comparison. 0.1 g of activated carbon was added to the 50 mL, 50 ppm As(V) samples, and the samples were allowed to stir for 6 h at 150 rpm. All samples were filtered using a 0.45 μm filter and analyzed on the MP-AES. Comparisons of the efficacy of the activated carbons were done by investigating the adsorption capacity of the material per gram (mg/g), normalized to a surface area of 1000 m^2 (mg/1000 m^2), and per cm^3 of micropores present in the material (mg/cm^3 micropores).

2.5.2. Kinetic Evaluations. Adsorption kinetics of the arsenic species onto the Commercial AC, Standard AC, Fe-loaded AC, Mn-loaded AC, and FeMn-loaded AC were obtained at times of 5, 10, 30, 45, 60, 120, and 360 min 0.1 g of the respective activated carbon was added to the 50 mL, 50 ppm As(V) samples and allowed to stir for the indicated time at 150 rpm before being filtered with a 0.45 μm filter. The filtrate was then analyzed using MP-AES analysis.

2.6. Arsenic(III) Evaluation. A 500 ppm stock solution of As(III) was prepared in deionized water using arsenic trioxide (As_2O_3). All samples and standards were prepared by serial dilution from the 500 ppm stock solution. Samples were prepared to a concentration of 50 ppm arsenic(III) with a final volume of 50 mL using deionized water to dilute the samples. 1 M HCl was used to bring the pH of the sample to 3.0.

Adsorption kinetics of the commercial AC, standard AC, and best-performing metal-loaded activated carbon (FeMn-loaded AC) for As(V) adsorption were obtained for arsenic(III) at times of 5 min, 10 min, 30 min, 45 min, 1 h, 2 h, 6 h, 24 h, 48 h, 72 h, 1 week, and 2 weeks. 0.1 g of the particular activated carbon was added to the 50 mL, 50 ppm As(III) samples and allowed to stir for their respective times at 150 rpm before being filtered using a 0.45 μm filter. The filtrate was then analyzed using MP-AES analysis.

3. RESULTS AND DISCUSSION

3.1. Nitrogen Adsorption Measurements. The standard activated carbon follows both a type I and a type II nitrogen adsorption isotherm, with a large increase in adsorption in the microporous region and a small increase in adsorption in the higher-pressure region. This indicates a highly microporous sample. Desorption seems to follow a type H4 hysteresis; however, the desorption isotherm does not fully close to the adsorption isotherm. The Fe-loaded, Mn-loaded, and commercial activated carbon materials follow a mixture of type I and type II nitrogen adsorption isotherms, similar to what is seen with the standard AC. The quantity of nitrogen adsorbed is less than that observed in the standard AC in the Fe-loaded, Mn-loaded ACs, and commercial AC, indicating a smaller pore volume in these materials. The isotherms for these samples also show a steeper curve near the saturation point, indicating a higher percentage of mesopores and macropores. These materials follow a type H4 hysteresis. Unlike the other activated carbon materials, the

https://doi.org/10.1021/acsomega.3c02078
ACS Omega 2023, 8, 29083–29100

Table 4. XPS Species Summary for Metal-Loaded Activated Carbons[26−32]

peak	species	binding energies (eV)	FeMn AC pre-As (% deconvolution)	FeMn AC post-As (% deconvolution)	Fe AC post-As (% deconvolution)	Mn AC post-As (% deconvolution)
Fe $2p_{3/2}$	Fe−metal	706.14	0.00	0.00	0.00	
	Fe_2O_3	709.75; 710.75; 711.75; 712.95; 714.05	32.18	1.66	16.73	
	$Fe_3O_4^{2+}$	708.45; 709.25	4.61	5.24	5.43	
	$Fe_3O_4^{3+}$	710.25; 711.25; 712.35; 713.45; 714.55	10.04	11.40	11.81	
	FeOOH	710.30; 711.30; 712.20; 713.30; 714.40	53.16	81.71	65.67	
Mn $2p_{3/2}$	Mn(0)	646.83	0.00	0.00		0.00
	Mn(II)−MnO	640.49; 640.53; 641.62; 642.87; 644.05	26.82	15.40		8.25
	Mn(III)−MnOOH	641.09; 641.57; 642.17; 643.48; 646.05	39.98	43.96		48.24
	Mn(IV)−MnO_2	642.00, 643.51, 643.66, 644.04, 644.87	33.20	40.64		43.51
As $2p_{3/2}$	arsenide	1322.90		0.00	0.00	0.00
	arsenic metal	1323.90		0.00	0.00	0.00
	As(III)	1327.00		77.26	85.87	100
	As(V)	1328.10		22.74	14.13	0.00

Table 5. XPS Survey Scan Breakdown for the Various Activated Carbon Materials

activated carbon	C at. %	O at. %	Mn at. %	Fe at. %	As at. %	other (Si, S, K) at. %
standard AC: pre-As exposure	78.88	17.44	0.10	0.29	0.43	2.86
standard AC: post-As exposure	60.89	30.45	0.17	0.03	4.06	4.40
FeMn-loaded AC: pre-As exposure	42.08	41.88	8.02	6.87	0.20	0.94
FeMn-loaded AC: post-As exposure	40.53	38.85	8.20	7.80	3.18	1.43
Fe-loaded AC: post-As exposure	28.90	49.36	0.21	6.80	7.51	7.21
Mn-loaded AC: post-As exposure	36.53	33.13	28.40	0.33	1.43	0.17

FeMn-loaded AC follows a type II adsorption isotherm where there is very little adsorption in the micropore region and a very large increase in the adsorption at higher relative pressures. The FeMn-loaded AC follows H3 hysteresis. The majority of the adsorption is occurring at higher relative pressures, indicating that the majority of the pore volume is made of mesopores and macropores. The FeMn-loaded AC shows the biggest difference due to blocking of the micropores and should show the most significant decrease in the micropore percentage. A summary of the pore information obtained from the nitrogen adsorption measurements is provided in Table 1. Figure 1 shows typical nitrogen isotherm plots of the activated carbons used within this study.

3.2. As(V) Efficacy Comparison. To compare the efficacy of the various activated carbons for arsenic(V) adsorption, 0.1 g of activated carbon was added to 50 mL samples of 50 ppm arsenic(V). Samples were stirred at 150 rpm for 6 h then filtered before elemental analysis of the filtrate.

3.2.1. Milligram Per Gram Adsorption Comparison. To compare the efficacy of the different activated carbon substrates, adsorption with respect to the amount of activated carbon added was compared in milligrams of arsenic(V) adsorbed per gram of activated carbon (mg/g). As shown in Figure 2, there was a dramatic improvement in the adsorption of arsenic after functionalization with the iron, manganese, and iron/manganese together.

All of the metal-modified activated carbons showed increased adsorption of arsenic(V) compared to the unmodified activated carbon. The single-metal-loaded activated carbons showed adsorptions of 4.86 ± 0.17 and 6.02 ± 0.16 mg/g for iron-loaded and manganese-loaded activated carbons, respectively, while the unmodified standard activated carbon showed an

Table 6. O 1s Deconvolution of the Metal-Loaded Activated Carbons[32,33]

species	BE	Fe-loaded AC (% deconvolution)	Mn-loaded AC (% deconvolution)	FeMn-loaded AC (% deconvolution)
C═O (aliphatic), −O−(C═O)	531.76	26.50	28.39	32.94
C═O (aromatic)	530.86	37.63	28.55	17.94
O_2/C	536.86	1.66	0.00	2.11
−O−(C═O)−O−(C═O)−O−(C═O)−	535.27	1.51	0.00	1.52
C−OH (aromatic)	533.16	4.34	0.00	0.00
O−(C═O)−C (aliphatic)	533.86	0.11	0.00	4.48
SiO_2	532.46	4.70	3.11	1.06
metal oxides	529.86	23.55	39.95	39.95

https://doi.org/10.1021/acsomega.3c02078
ACS Omega 2023, 8, 29083−29100

Table 7. Summary of the Pseudo-First- and Pseudo-Second-Order Kinetic Modeling for the Activated Carbons Used for Arsenic(V) Adsorption

activated carbon	pseudo-first- or pseudo-second-order model	model equation	linearity (R^2) of the model	k value	q_e value	q_e experimental
commercial AC	first	$y = -7.9 \times 10^{-3}x + 1.0677$	0.8550	7.9×10^{-3}	2.91	8.46 ± 0.34
	second	$y = 0.1161x + 1.2845$	0.9968	0.0105	8.61	
standard AC	first	$y = -0.0135x + 0.2616$	0.9955	0.0135	1.30	2.08 ± 0.11
	second	$y = 0.4605x + 9.0164$	0.9967	0.0235	2.17	
Fe-loaded AC	first	$y = -9.9 \times 10^{-3}x + 0.5587$	0.9330	9.9×10^{-3}	1.75	4.86 ± 0.17
	second	$y = 0.2019x + 2.1041$	0.9980	0.0190	4.95	
Mn-loaded AC	first	$y = -0.0105x + 1.1712$	0.9953	0.0105	3.23	6.02 ± 0.16
	second	$y = 0.1599x + 3.0148$	0.9948	8.5×10^{-3}	6.25	
FeMn-loaded AC	first	$y = -6.7 \times 10^{-3}x + 1.532$	0.8416	6.7×10^{-3}	4.63	12.88 ± 0.58
	second	$y = 0.0762x + 0.9768$	0.9951	5.9×10^{-3}	13.12	

Table 8. Summary of the Pseudo-First- and Pseudo-Second-Order Kinetic Modeling for the Activated Carbons Used for Arsenic(III) Adsorption

activated carbon	pseudo-first- or pseudo-second-order model	model equation	linearity (R^2) of the model	k value	q_e value	q_e experimental
commercial AC	first	$y = -8.23 \times 10^{-4}x + 0.9304$	0.9515	8.23×10^{-4}	2.54	2.92 ± 0.12
	second	$y = 0.3399x + 80.979$	0.9986	0.0123	2.94	
standard AC	first	$y = -2.87 \times 10^{-4}x + 0.7332$	0.9450	2.78×10^{-4}	2.08	3.59 ± 0.43
	second	$y = 0.2789x + 71.431$	0.9981	0.0140	3.59	
FeMn AC	first	$y = -3.85 \times 10^{-4}x + 1.4759$	0.8701	3.85×10^{-4}	4.37	9.28 ± 0.61
	second	$y = 0.1076x + 13.34$	0.9997	0.0750	9.29	

Table 9. Comparison of PC-Derived Activated Carbons for As(V) and As(III) Adsorption with Other Studies in the Literature

material	As(V) adsorption capacity (mg/g)	As(III) adsorption capacity (mg/g)	pH	surface area (m^2/g)	references
standard AC	2.08 ± 0.11	3.59 ± 0.43	3.0, 3.0	975 ± 19	this study
Fe-loaded AC	4.86 ± 0.17		3.0, 3.0	748 ± 13	this study
Mn-loaded AC	6.02 ± 0.16		3.0, 3.0	487 ± 15	this study
FeMn-loaded AC	12.88 ± 0.58	9.28 ± 0.61	3.0, 3.0	397 ± 11	this study
commercial AC	8.46 ± 0.34	2.92 ± 0.12	3.0, 3.0	1329 ± 38	this study
granular ferric hydroxide	29.07		6.0	306	9
MIRESORB	50.38		6.0	233	
UiO-66-NDC/GO	147.06		3.0	279.77	10
saxaul ash	4.203		7.0	not reported	11
diatom silica shells		10.99	4.0	7.30 ± 0.03	13
iron oxide/12 × 40 granular coconut AC composite	0.4123		2.0	678.3	14
	1.0389		5.0		
	2.0716		10.0		
biosorbent egg shell	8.43 ± 2.1	11.69 ± 2.5	4.1, 7.0	7.91 ± 0.49	41
biosorbent java plum seed	4.62 ± 0.43	4.63 ± 0.65	5.3, 7.0	6.99 ± 0.61	
biosorbent water chestnut shell	7.73 ± 0.9	9.61 ± 1.21	4.1, 7.0	6.91 ± 0.42	
biosorbent corn cob	5.71 ± 0.32	4.33 ± 0.76	6.0, 7.0	4.16 ± 0.57	
biosorbent tea waste	4.92 ± 1.21	7.36 ± 1.28	4.1, 7.0	4.03 ± 0.61	
biosorbent pomegranate peel	4.50 ± 0.42	5.57 ± 1.28	4.1, 9.0	3.96 ± 0.72	

adsorption of 2.08 ± 0.11 mg/g. By loading the combination of iron and manganese onto the surface, the adsorption efficiency is even more dramatically improved, with arsenic adsorption reaching 12.88 ± 0.58 mg/g. The commercial activated carbon was also tested after functionalization with the iron−manganese mixture. An improvement in the adsorption capacity was observed from 8.46 ± 0.34 to 15.55 ± 1.09 mg/g. This was done to prove that surface functionalization plays a key role in adsorption and that the adsorption capacity of a material with a high surface area can be improved by modification of the surface functionalization, even at the cost of a decrease in the specific surface area. Since this study aims to focus on the modification of the PC activated carbon, the functionalization of the commercial activated carbon will not be investigated further.

3.2.2. Arsenic(V) Adsorption on Normalized Surface Area Substrates. The arsenic species adsorption is also impacted by the variation in specific surface area of the activated carbon substrates, particularly as the loading of iron and manganese species significantly reduces the specific surface area of the substrate. Similar to the mg/g comparison, the arsenic(V) adsorption efficiencies of each activated carbon were calculated but then normalized to a surface area of 1000 m^2. Table 2 shows the adsorption of arsenic(V) for the five activated carbon materials, each normalized to a surface area of 1000 m^2. The

https://doi.org/10.1021/acsomega.3c02078
ACS Omega 2023, 8, 29083−29100

Table A1. MP-AES Operating Conditions for the Analysis of Arsenic(V) and Arsenic(III)

instrument parameter	operating condition
spray chamber	cyclonic single-pass
sample uptake (s)	30
stabilization (s)	15
read time (s)	10
number of replicates	3
background correction	auto
wavelength (nm)	188.979
ignition gas	argon
carrier gas	nitrogen
carrier gas flow rate (L/min)	0.70
calibration fit	linear
acceptable linear tolerance	≥0.9900
calibration error	10%

metal-loaded activated carbons, despite having a lower surface area, have a comparable, or better, adsorption than the high surface area commercial activated carbon. This demonstrates the significance of the surface functionality of the activated carbon substrate on the arsenic adsorption over the surface area.

The reduction of the activated carbon surface area due to metal impregnation of the activated carbon surface is expected. With the inclusion of the metal species, the density of the material increases, so there will be a small decrease in specific surface area due to this effect. A more significant impact on the surface area occurs when metal species are added to the surface of the activated carbon; the particles can enter the pores of the activated carbon, clogging the pores at the neck of an opening. This pore filling will make the area deeper within the pores inaccessible, effectively removing the surface area that these pores would provide and significantly lowering the surface area of the material. XPS of the activated carbon samples showed that iron loading on the iron-loaded sample made up 6.8 at. % (25 wt %) of the activated carbon and that manganese loading in the manganese-loaded sample made up 28.4 at. % (64.5 wt %) of the activated carbon. This corresponds well with the observed decrease in surface area as the higher loading of the manganese filled more of the pores in the manganese-loaded activated carbon, blocking off more surface area than what was observed in

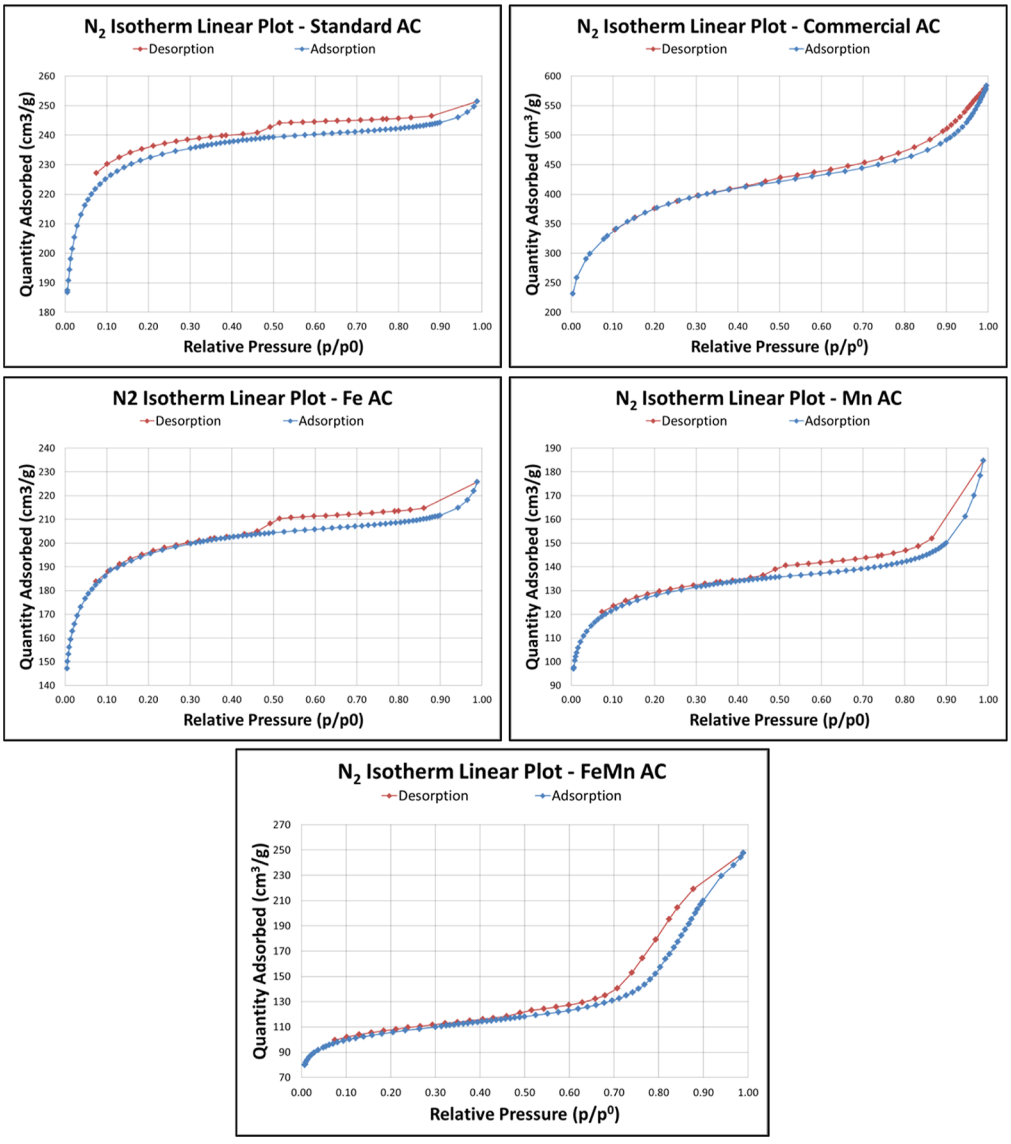

Figure 1. Nitrogen adsorption isotherm and hysteresis plots of the standard, commercial, Fe-loaded, Mn-loaded, and FeMn-loaded activated carbons.

https://doi.org/10.1021/acsomega.3c02078
ACS Omega 2023, 8, 29083−29100

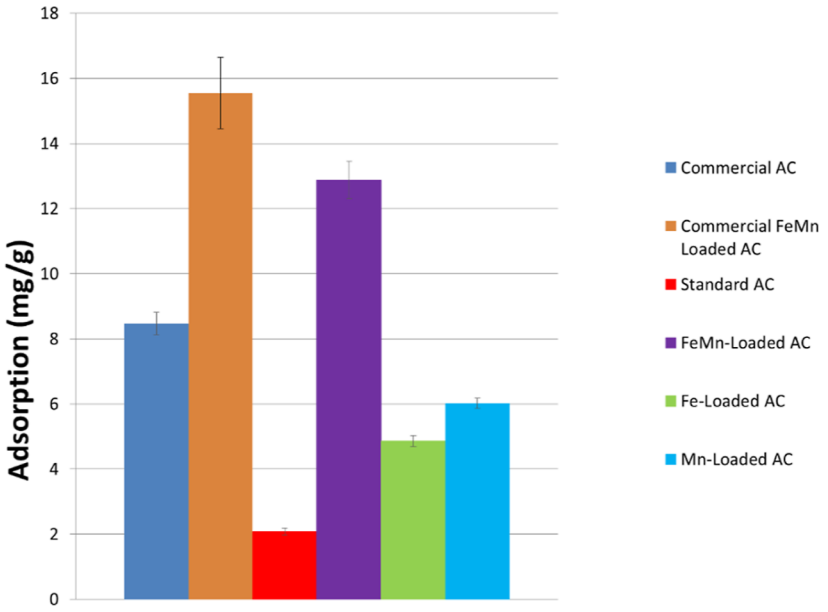

Figure 2. Comparison of various activated carbons investigating the adsorption efficiency of arsenic(V) after a 6 h exposure time.

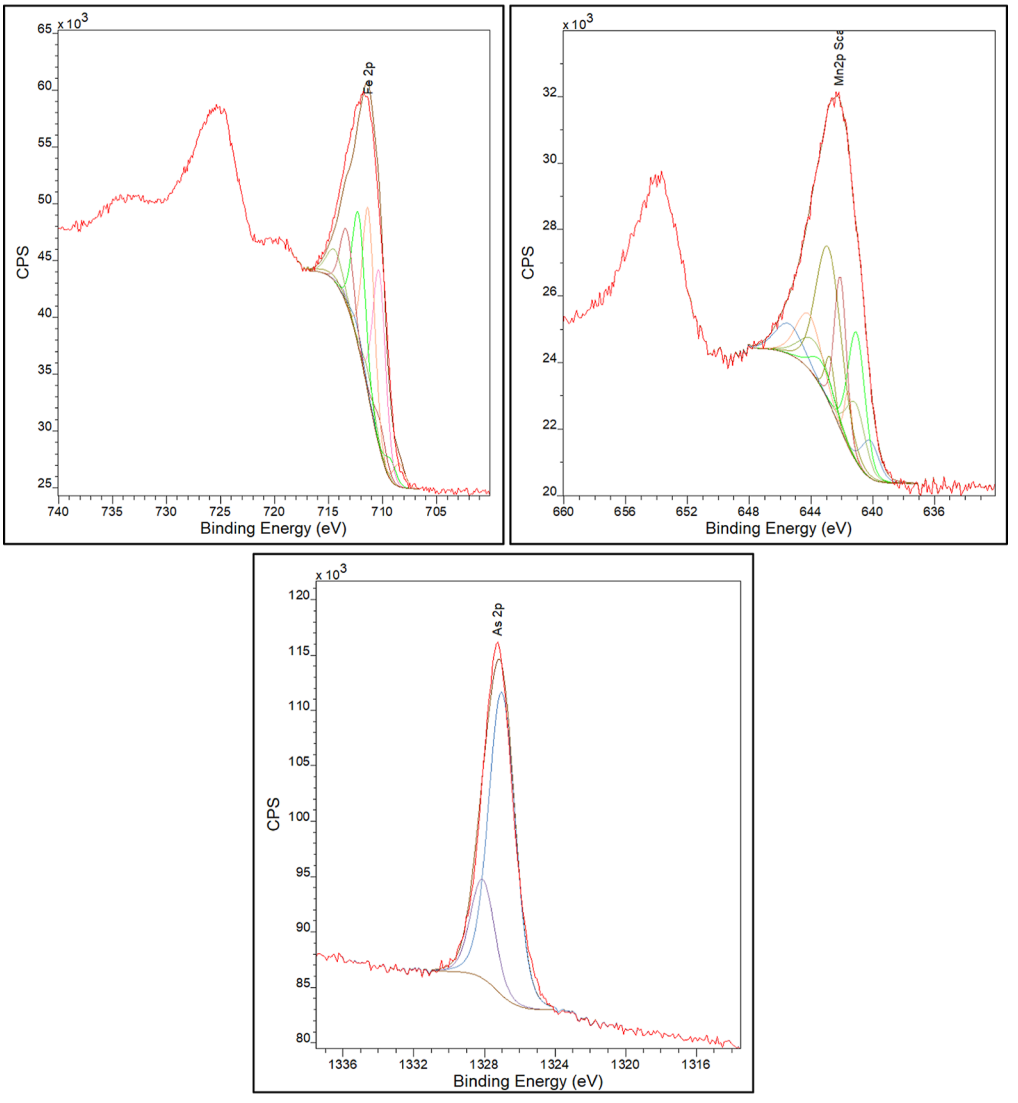

Figure 3. Deconvolution of the Fe (top left), Mn (top right), and As (bottom) XPS peaks in the FeMn-loaded AC, post-As exposure.

https://doi.org/10.1021/acsomega.3c02078
ACS Omega 2023, 8, 29083−29100

the iron-loaded activated carbon. This is also consistent with the nitrogen adsorption measurements presented in Table 1, which indicate that the Mn-loaded AC has less pore volume than the other activated carbons and a larger average pore size. This would indicate that the manganese is blocking the majority of the micropores, decreasing the available surface area, pore volume, and increasing the average pore size. XPS of the FeMn-loaded AC showed that total metal loading on the activated carbon was 16 at. % (46.8 wt %), consisting of 8.2 at. % (24.1 wt %) iron and 7.8 at. % (22.7 wt %) manganese. This binary metal system also decreases the surface area of the activated carbon. Interactions between the iron and manganese likely produce larger mixed metal precipitates that block pores earlier in the pore channel, causing larger amounts of micropore volume to be inaccessible and decreasing surface area further than the single metal system of either iron or manganese. This is consistent with the nitrogen adsorption measurement results in Table 1 that show the much larger average pore size of the FeMn-loaded AC. The total pore volume is larger than that of the single metal-loaded activated carbons, likely due to the very large macropores driving the pore volume up.

3.2.3. Arsenic(V) Adsorption on Normalized Microporosity Substrates. Similar to the surface area normalization, the normalization of the adsorption relative to the microporosity of the various activated carbons was investigated. Adsorption of arsenic(V) was normalized to 1 cm^3 of micropore volume so that adsorption per micropore volume could be analyzed. Trends in this graph would indicate the influence of microporosity on the adsorption and whether microporosity is a driving factor for arsenic(V) adsorption in these activated carbons. Table 3 summarizes the microporosities of the activated carbons and their respective adsorption capacities normalized to microporosity.

No observable trends are found with respect to adsorption capacity normalized to the microporosity of a material; therefore, it is concluded that the microporosity of a given material is not a driving factor in the adsorption of arsenic(V) and that the surface functionality of the material is much more important.

3.3. XPS Characterization of Metal-Modified Activated Carbons Pre- and Post-arsenic Adsorption. The deconvolution, species assignments, and percent of total peak area for the Fe $2p_{3/2}$, Mn $2p_{3/2}$, and As $2p_{3/2}$ XPS peak signals for the FeMn AC pre- and post-arsenic exposure, the Fe-loaded AC post-arsenic exposure, and the Mn-loaded AC post-arsenic exposure are shown in Table 4. Note that the Fe_2O_3, $Fe_3O_4^{2+}$, $Fe_3O_4^{3+}$, FeOOH, MnO, MnOOH, and MnO_2 species identification is made more complex by the well-known XPS multiplet splitting for these iron and manganese species.[26−28] XPS spectra of Fe 2p, Mn 2p, and As 2p deconvolution of the FeMn-loaded AC post-arsenic adsorption are depicted in Figure 3 as an example of the deconvolution of the relevant peaks for each activated carbon sample. The Fe 2p, Mn 2p, and As 2p XPS spectra for the FeMn-loaded AC pre-arsenic exposure, Fe-loaded AC, and Mn-loaded AC can be found in Appendix B, Figures B1−B3.

One possible explanation of the increased arsenic adsorption observed in the metal-loaded activated carbons is arsenide formation. If arsenide formation was the reason for the increased adsorption, the XPS spectra of the arsenic $2p_{3/2}$ peak would show arsenides at a BE of 1322.9 eV.[29] Since no peaks are present in this region, arsenide formation does not occur, and the enhanced arsenic adsorption observed for Fe, Mn, and FeMn treated AC must be through a different mechanism. Based on our characterization of the pre- and post-arsenic exposure AC samples with and without iron and manganese loading, we have concluded that an oxidation/reduction reaction is likely occurring. This is consistent with the XPS results, particularly for the arsenic $2p_{3/2}$ peaks, which show that the arsenic species present on the surface of the activated carbon materials are reduced to arsenic(III). Table 4 provides the XPS deconvolution results for the metal-loaded activated carbon materials, both pre- and post-arsenic adsorption. Table 5 provides the XPS survey

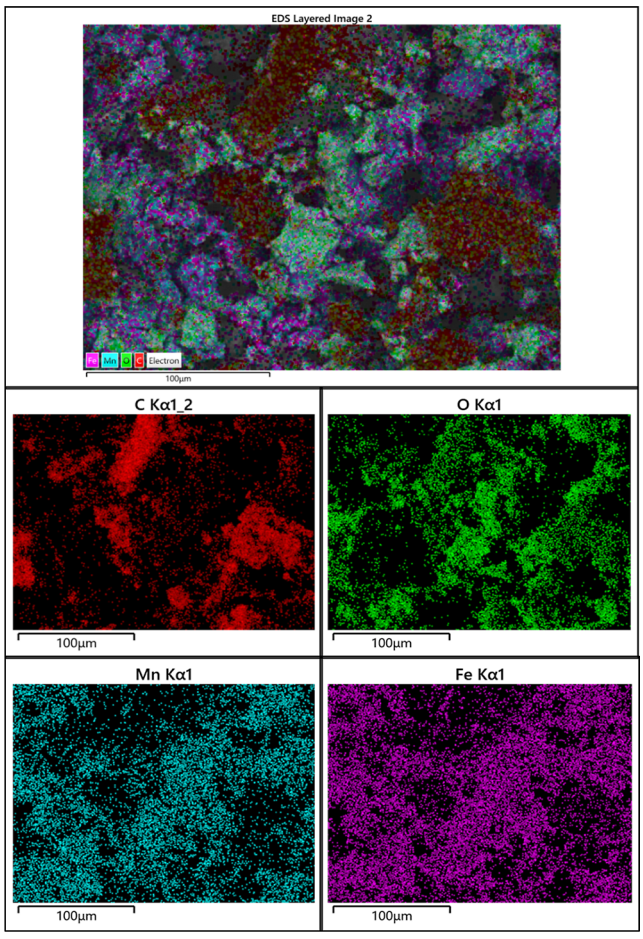

Figure 4. Elemental distribution mapping of carbon (middle left), oxygen (middle right), manganese (bottom left), and iron (bottom right) present within the FeMn-loaded activated carbon. A layered distribution map of the surface's elemental composition is shown at the top.

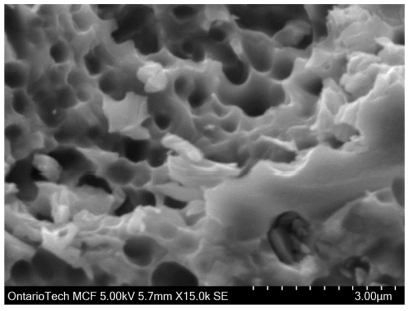

Figure 5. SEM imaging (magnification ×15,000) of the standard activated carbon to show the smallest pore size visible with the SEM images obtained.

https://doi.org/10.1021/acsomega.3c02078
ACS Omega 2023, 8, 29083−29100

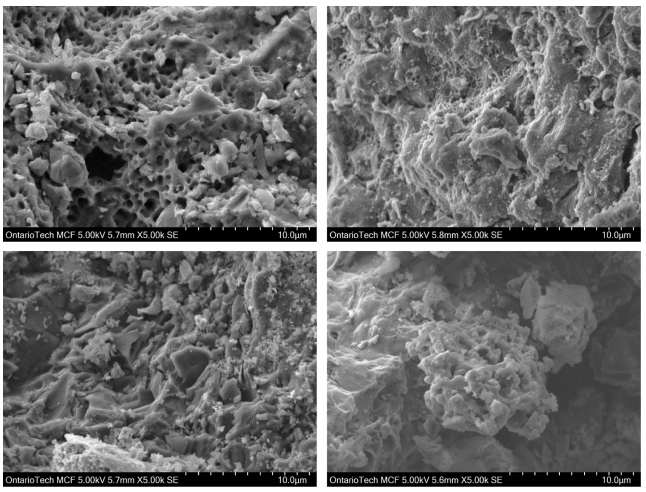

Figure 6. SEM imaging (magnification ×5000) of the standard (top left), Fe-loaded (top right), Mn-loaded (bottom left), and FeMn-loaded activated carbons used in this study.

scan results with the elemental composition of the species listed as atomic percent.

3.4. Energy-Dispersive X-ray Spectroscopy. Energy-dispersive X-ray spectroscopy (EDS) was performed on the activated carbon samples to investigate the elemental distribution on the surface of the materials. In the Fe-loaded AC, EDS shows that the iron on the activated carbon is distributed fairly evenly across the surface. There are small clumps of iron located on the surface in no particular pattern. This would be consistent with the small decrease in surface area observed between the standard activated carbon and the Fe-loaded AC. Similarly, the Mn-loaded AC shows fairly even distribution across the surface of the material but does show larger concentrations of manganese present in the pores around high concentrations of carbon. Again, this is consistent with the observed decrease in surface area, where a much larger decrease is observed due to the filling of the pores. In the FeMn-loaded AC, both iron and manganese distributions are heavily concentrated in the pores and spaces between clusters of carbon. This would be consistent with the significant decrease in the surface area as the iron and manganese block the surface within these pores.

Oxygen distribution in the iron-only sample seems to be mostly concentrated with the small carbon clusters and small clusters of iron oxides present in the sample. This is consistent with the XPS of the iron-only sample, which shows the oxygen deconvolution is made primarily of carbon-oxygen species, with

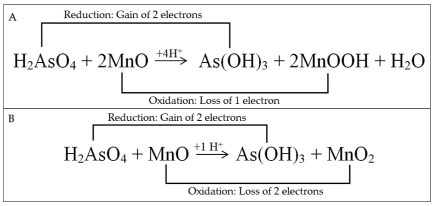

Figure 8. (A) Shows the redox reaction between As(V) and Mn(II), where As(V) is reduced to As(III) and Mn(II) is oxidized to Mn(III). (B) Shows the redox reaction between As(V) and Mn(II), where As(V) is reduced to As(III) and Mn(II) is oxidized to Mn(IV).

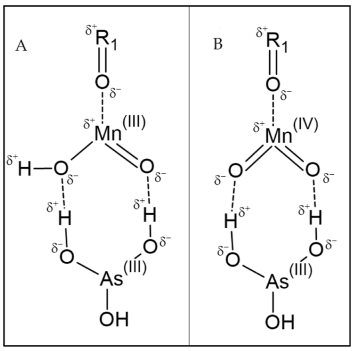

Figure 9. (A) Shows the product of reaction (1), where MnO is oxidized to MnOOH. (B) Shows the product of reaction (2), where MnO is oxidized to MnO_2. As(III) is physisorbed to the Mn-loaded surface through hydrogen bonding.

metal oxides making up only 23.55% of the oxygen species present on the surface. The oxygen distribution in the manganese-only sample seems to be mostly concentrated to the carbon clusters, with larger clusters of manganese oxides present compared to the iron-only sample. This is again consistent with the XPS of the manganese-only samples, where the majority of the oxygen deconvolution is carbon−oxygen species and the metal oxides make up 39.95% of the oxygen within the sample, indicating slightly larger clusters of metal oxides compared to the iron-only sample. The FeMn-loaded AC shows high concentrations of oxygen present where the carbon clusters are located but also significant concentrations of metal-oxide clusters. This is consistent with the XPS of the FeMn-loaded AC, where the majority of the oxygen deconvolution is carbon-oxygen species, with metal oxides making up 39.95% of the oxygen species as a mixture of clusters of iron-oxides and manganese-oxides. Figure 4 shows the EDS images for the

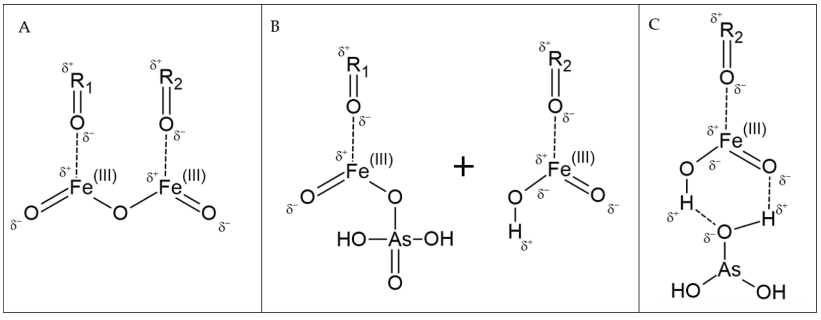

Figure 7. (A) Shows the iron physisorbed to the surface of the activated carbon. (B) Shows the two iron products, FeOOH, and the intermediate FeO−O−AsH_2O_3, formed as a result of the exposure to arsenic. (C) Shows the reduced As(III), as a result of the electron flow from the activated carbon through the iron, physisorbed to the iron-loaded surface through hydrogen bonding.

https://doi.org/10.1021/acsomega.3c02078
ACS Omega 2023, 8, 29083−29100

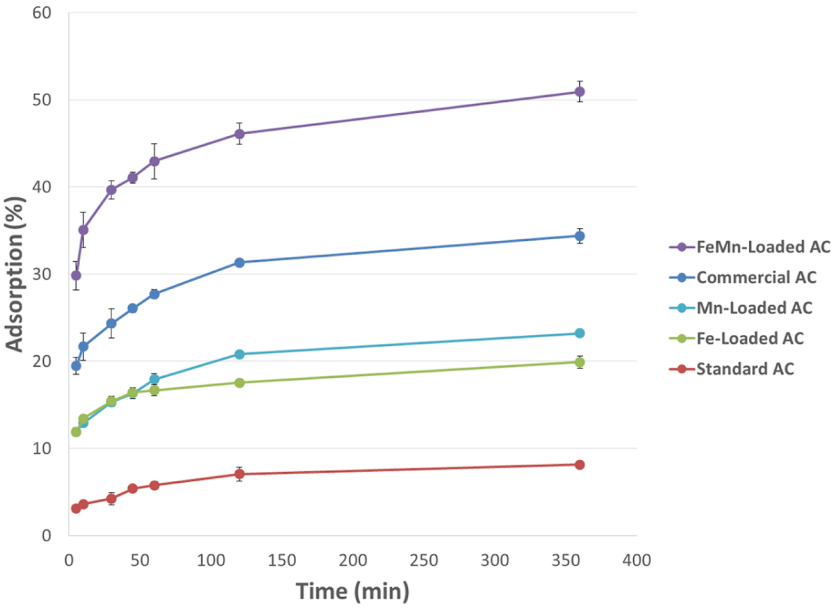

Figure 10. Kinetics curves of As(V) adsorption for the various activated carbons investigated. Arsenic adsorption is given in percent adsorption with a maximum adsorption (i.e., 100%) of 25 mg/g.

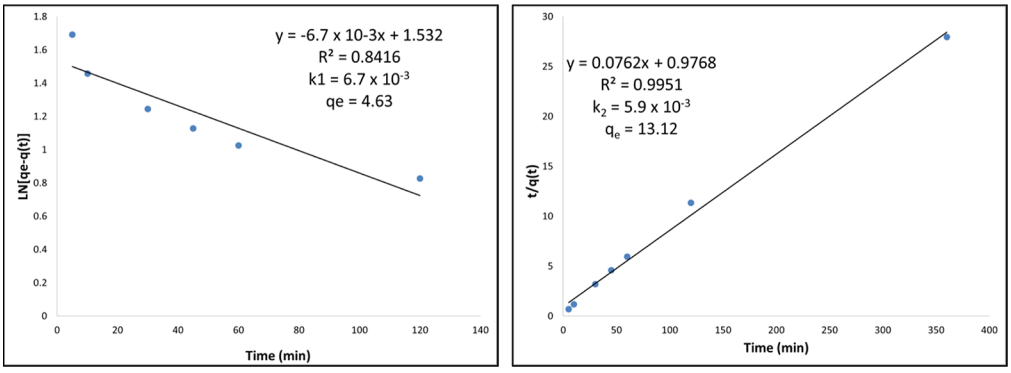

Figure 11. Pseudo-first (left) and pseudo-second (right) order kinetic modeling of the As(V) adsorption using the FeMn-loaded AC.

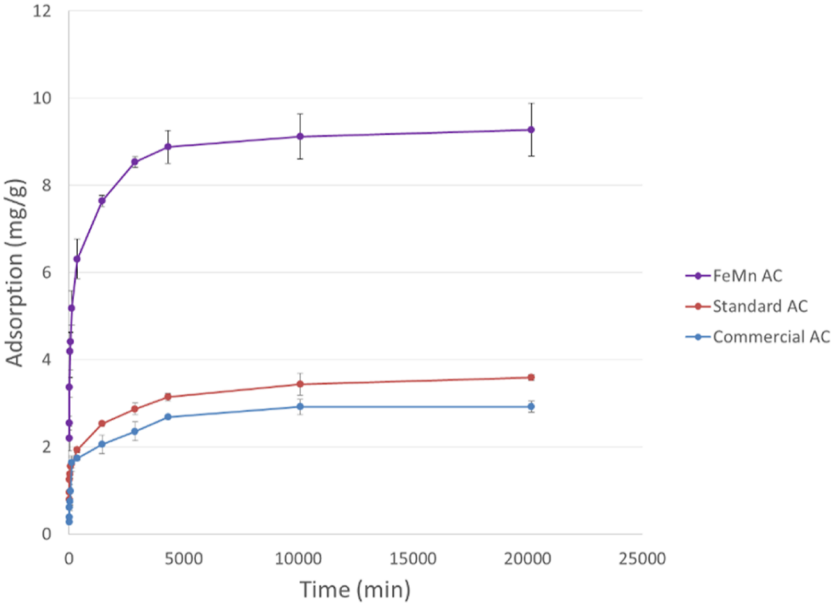

Figure 12. Kinetics curves of the As(III) adsorption using the FeMn-loaded, standard, and commercial activated carbons.

https://doi.org/10.1021/acsomega.3c02078
ACS Omega 2023, 8, 29083−29100

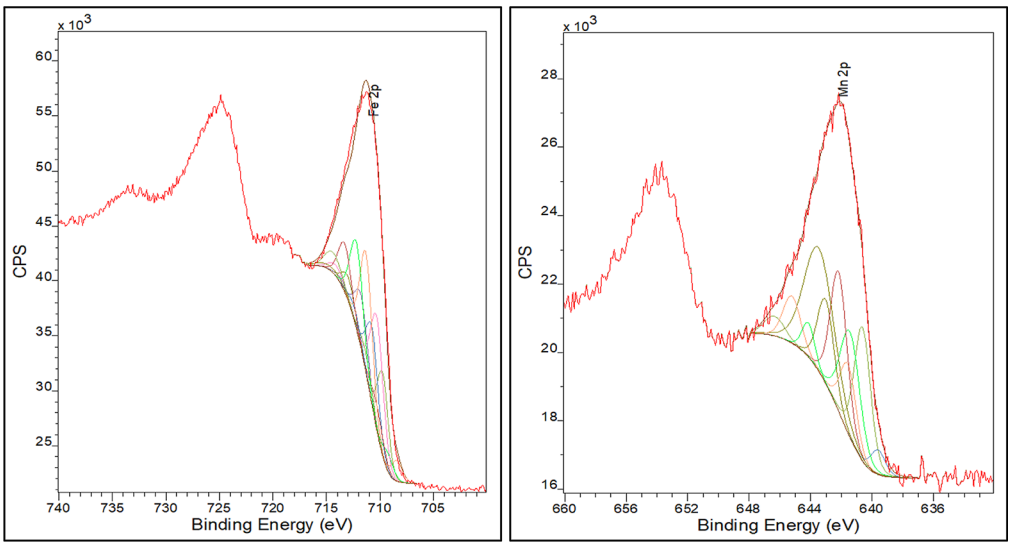

Figure B1. XPS deconvolution of the Fe 2p (left) and Mn 2p (right) peaks in the FeMn-loaded AC pre-exposure to arsenic.

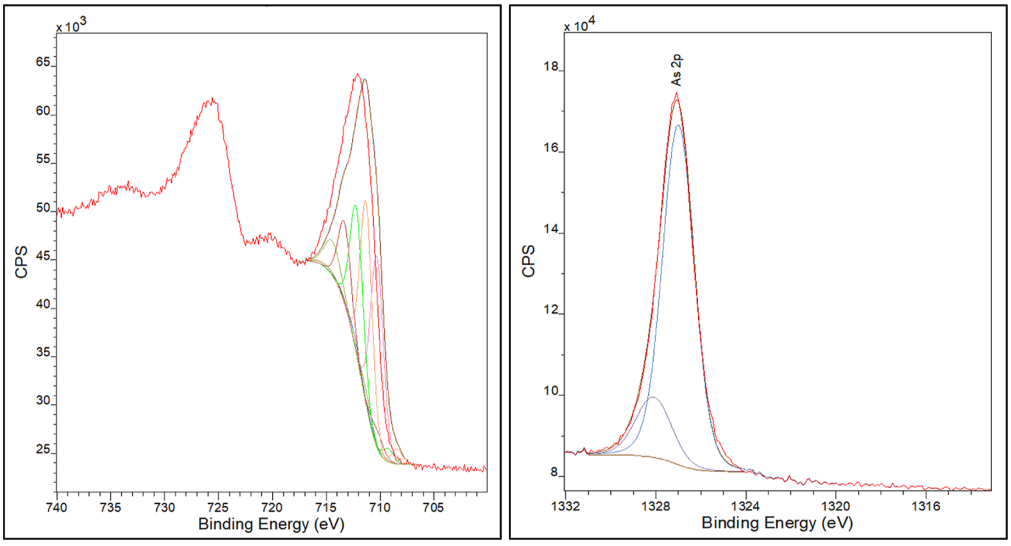

Figure B2. XPS deconvolution of the Fe 2p (left) and As 2p (right) peaks in the Fe-loaded AC.

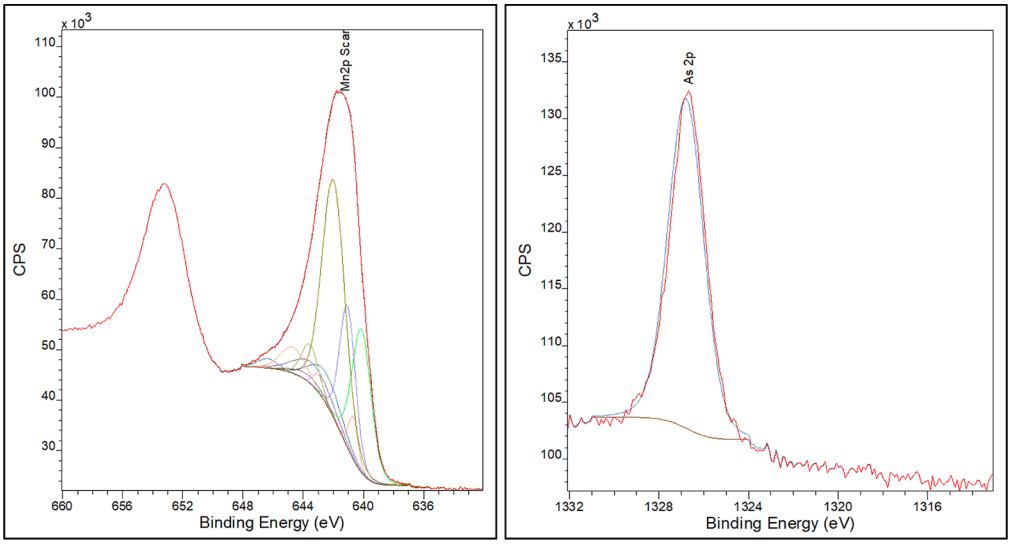

Figure B3. XPS deconvolution of the Mn 2p (left) and As 2p (right) peaks in the Mn-loaded AC.

https://doi.org/10.1021/acsomega.3c02078
ACS Omega 2023, 8, 29083−29100

FeMn-loaded AC at a magnification of 500 times. Appendix C, Figures C1−C3 shows the EDS images for the standard, Fe-loaded, and Mn-loaded activated carbons. The XPS deconvolution of the oxygen species is presented in Table 6, below.

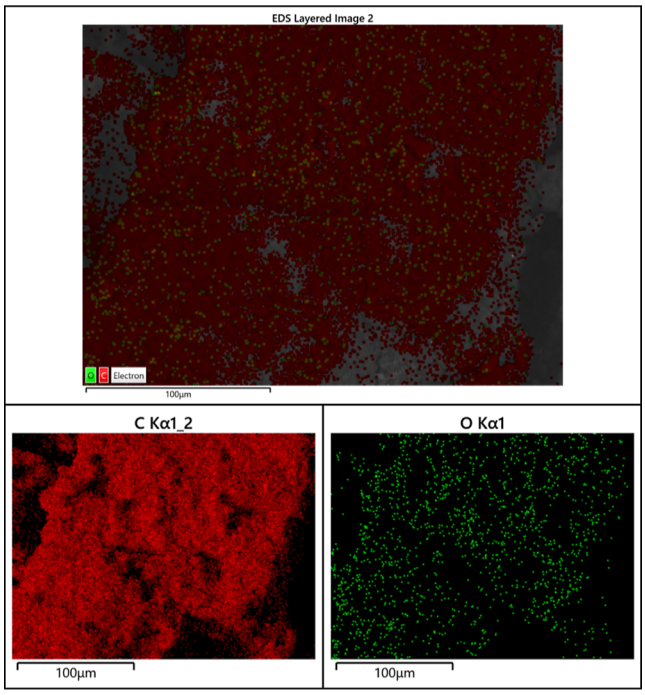

Figure C1. Elemental distribution mapping of carbon (bottom left) and oxygen (bottom right) present within the standard activated carbon at 500× magnification. A layered distribution map of the surface's elemental composition is shown at the top.

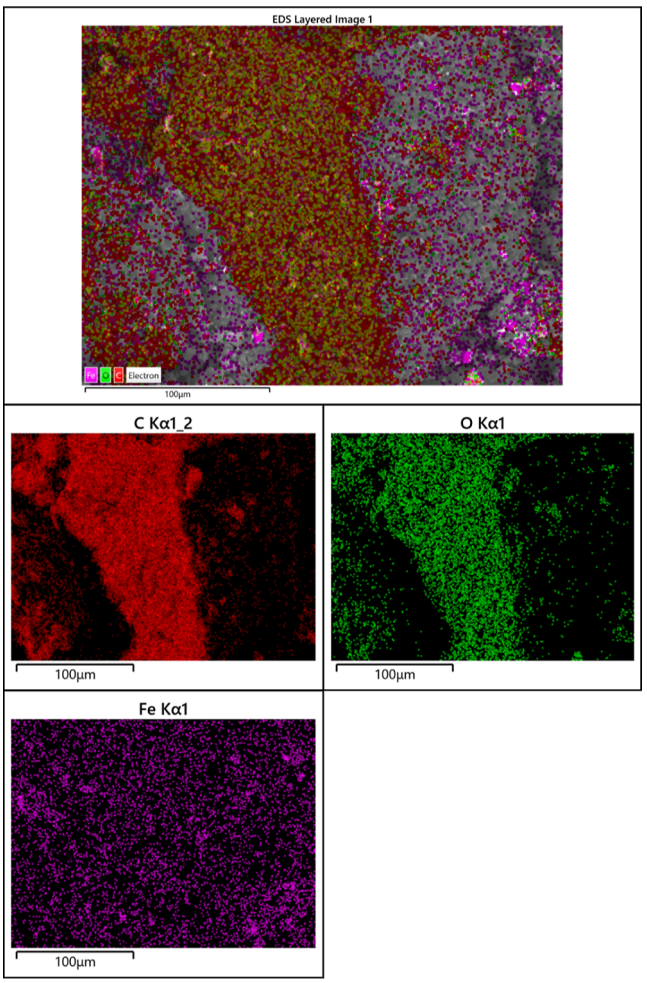

Figure C2. Elemental distribution mapping of carbon (middle left), oxygen (middle right), and iron (bottom) present within the Fe-loaded activated carbon at 500× magnification. A layered distribution map of the surface's elemental composition is shown at the top.

3.5. Scanning Electron Microscopy Images. Scanning electron microscopy (SEM) images of the activated carbon materials were obtained at magnifications of between 150 and 15,000 times. The SEM images of the standard activated carbon show the extremely porous surface of the material. All pores that are observed in the SEM images are macropores, as the smallest visible pore (in the standard AC 15,000 magnification) is approximately 250 nm in diameter, as shown in Figure 5.

The SEM images of the Fe-loaded (Figure 6) AC show a much less porous surface. Pores and cracks in the surface are visible, with the iron loaded onto the surface blocking much of the pore structure. This is consistent with the decreased pore volume observed in the Fe-loaded sample. The SEM images of the Mn-loaded AC show almost no visible pores as the manganese blocks almost all of the pore structure; again, this is consistent with the observed decrease in the pore volume from the nitrogen adsorption measurements. The SEM images of the FeMn-loaded AC show a significant amount of macropores within the material, with the material itself being made of much smaller particles than the other activated carbons, which consisted of larger chunks.

3.6. Proposed Mechanisms. *3.6.1. Iron-Based Arsenic Adsorption.* Investigating the XPS results presented in Table 4, it can be observed that the iron species on the surface of the pre-arsenic-exposed FeMn AC are mainly Fe_2O_3 and FeOOH species, comprising 32 and 53% of the iron species, respectively. After arsenic exposure, these percentages significantly change to 1.7% Fe_2O_3 and 82% FeOOH. Speciation of the arsenic(V) in a pH 3.0 solution is known to be $H_2AsO_4^-$, and XPS of the As $2p_{3/2}$ peak post-adsorption shows that arsenic(V) is significantly reduced to arsenic(III) during the adsorption process.

During the functionalization process, iron is loaded onto the surface of the activated carbon and is physisorbed to the surface through dipole−dipole intermolecular forces, as shown in Figure 7A where *R* represents the activated carbon. The highly oxophilic character of iron would be an ideal surface for the negatively charged oxygen of the arsenic to form an iron-oxide bond, breaking the Fe_2O_3 species into an $FeOO^-$ that can be hydrolyzed to FeOOH and an intermediate species where arsenic and iron are bound through a shared oxygen, as shown in Figure 7B. This intermediate would be quickly broken down by electrons in the activated carbon using the iron as a conductor through which the electrons can freely flow to the arsenic and reduce the arsenic species from arsenic(V) to arsenic(III). In this case, the iron acts only as a pathway for the electrons to flow, with the activated carbon itself acting as the reducing agent. This is known based on the XPS speciation of iron, where Fe(III) remains as Fe(III), indicating that it is not acting as the reducing agent but rather as a shuttle for the electrons to reach the arsenic. In this reduction process, the chemical bond of the arsenic would be broken from the shared oxygen on the iron species, and the reduced arsenic(III) species would be physisorbed through

https://doi.org/10.1021/acsomega.3c02078
ACS Omega 2023, 8, 29083−29100

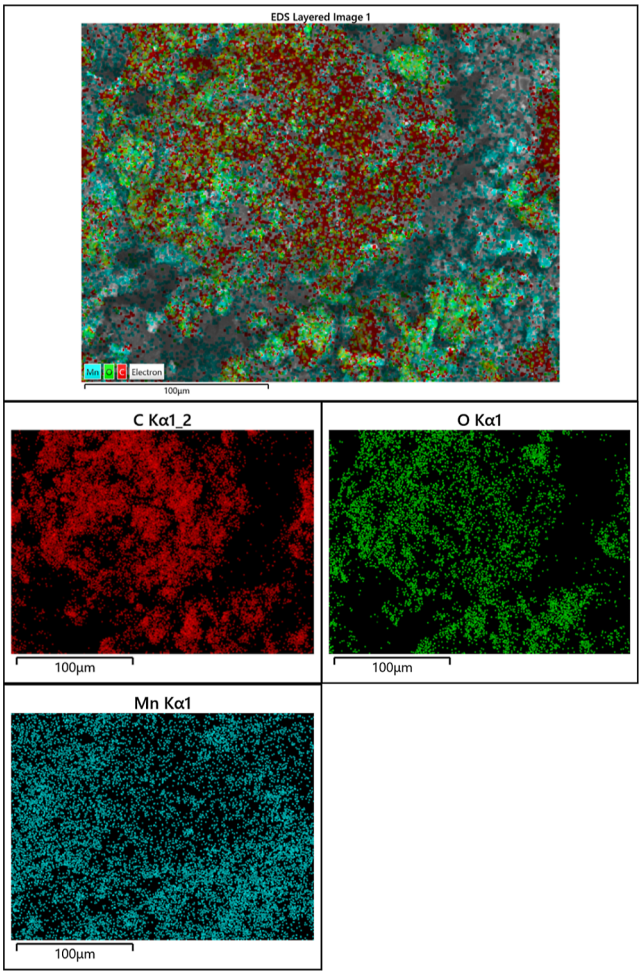

Figure C3. Elemental distribution mapping of carbon (middle left), oxygen (middle right), and manganese (bottom) present within the Mn-loaded activated carbon at 500× magnification. A layered distribution map of the surface's elemental composition is shown at the top.

hydrogen bonding to the iron-loaded surface of the activated carbon, as observed in Figure 7C.

This series of events would be consistent with the decrease in the Fe_2O_3 species and the increase in the FeOOH species observed due to the adsorption of arsenic. It would also be consistent with the observed reduction of the arsenic(V) species to arsenic(III) observed in the XPS. Finally, it would explain how the arsenic(V) species is being reduced to arsenic(III) without observing a change in the iron speciation; the iron is simply being used as a conduit for electrons to flow from the activated carbon to the arsenic. The higher adsorption capacity observed in this study due to the iron loading on the activated carbon surface is consistent with previous literature on the adsorption of arsenic using iron nanoparticles, where iron oxide nanoparticles are shown to be highly efficient adsorbents for both arsenic(III) and arsenic(V).[34,35]

3.6.2. Manganese-Based Mechanism. Investigating the XPS results in Table 4, it can be observed that a significant decrease in the MnO species is observed, from 27% pre-exposure to 15% post-exposure. This decrease in the MnO species leads to an increase in both the MnOOH and MnO_2 species present on the activated carbon. In a fashion similar to the iron-based arsenic adsorption, during functionalization of the activated carbon, MnO is physisorbed to the activated carbon surface through dipole−dipole interactions. Unlike iron, in the case of manganese, two different processes can be observed. The first process is the oxidation of manganese(II) to manganese(III). In this process, the arsenic takes one electron from two different manganese molecules, as observed in the redox reaction equation shown in Figure 8A. This reaction would use the manganese as a reducing agent to reduce arsenic(V) to arsenic(III) that would be physisorbed through hydrogen bonding to the MnOOH species that would be formed from this process, as observed in Figure 9A.

The second process is the oxidation of manganese(II) to manganese(IV). In this process, the arsenic would take both electrons from a manganese molecule, as observed in the redox reaction equation shown in Figure 8B. This process would use the manganese as a reducing agent to reduce arsenic(V) to arsenic(III) that would be physisorbed through hydrogen bonding to the MnO_2 species that would be formed from this process, as observed in Figure 9B. This series of events would be consistent with the decrease observed in the MnO species and the increases observed in the MnOOH and the MnO_2 species. It would also be consistent with the observed reduction of arsenic(V) to arsenic(III).

Unlike the iron-based adsorption proposed above, the activated carbon is not involved in the redox process of adsorption as is observed in the iron-based adsorption. The activated carbon, in this case, is providing an important surface on which the chemistry can occur so that the arsenic can be adsorbed and removed from solution.

3.7. Arsenic Kinetics. *3.7.1. Arsenic(V) Kinetics Curves.* The adsorption kinetics of arsenic(V) using metal-loaded activated carbons, standard activated carbon, and commercial activated carbon were evaluated, and the results are shown in Figure 10. For each of the carbon materials, adsorption of the arsenic(V) reaches equilibrium after 6 h. The standard activated carbon shows the lowest adsorption capacity, reaching 8.13 ± 0.16% of the total possible adsorption after 6 h. The Fe-loaded AC and Mn-loaded AC both show higher adsorption capacities than the standard AC, showing that metal loading of the surface does improve the adsorption capacity of the activated carbon. The Fe-loaded and Mn-loaded activated carbons show significant improvements over the standard activated carbon with regards to the adsorption of arsenic both at short and long stirring times, reaching 19.90 ± 0.71 and 23.21 ± 0.23%, respectively after 6 h.

The combined iron−manganese-loaded activated carbon shows the highest adsorption capacity, with adsorption after 6 h reaching 50.93 ± 1.17% of the total possible adsorption. This shows a significant improvement over both the standard activated carbon and the single-metal-loaded activated carbons. The binary system of the iron−manganese-loaded activated carbon works together, using all of the adsorption mechanisms presented above in the adsorption process, allowing the adsorption capacity to increase more than that of the single-metal-loaded activated carbon materials.

3.7.2. Arsenic(V) Kinetic Modeling. Pseudo-first-order and pseudo-second-order kinetic modeling were performed on each of the activated carbons following adsorption kinetic modeling. Modeling was performed using the data provided in Figure 10. A review article by Tran et al.[36] provides information regarding modeling of kinetic data. Tran et al. mention the original work by Lagergren in 1898, who first presented the first-order rate

https://doi.org/10.1021/acsomega.3c02078
ACS Omega 2023, 8, 29083−29100

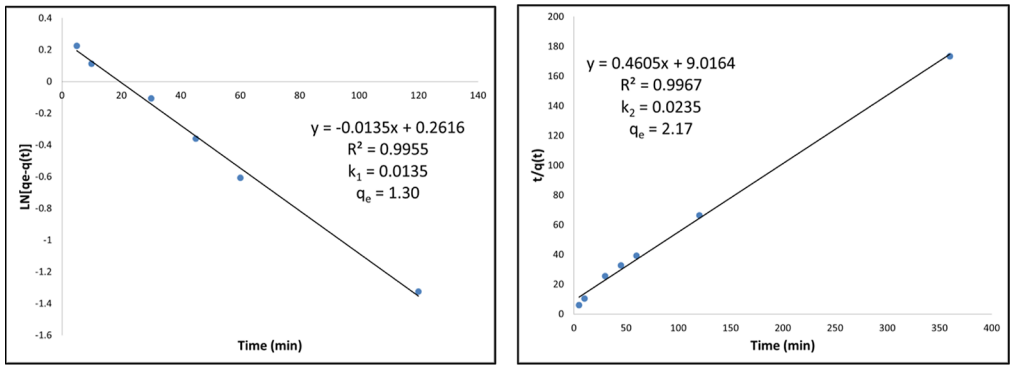

Figure D1. Pseudo-first (left) and pseudo-second (right) order kinetic models for the adsorption of As(V) using the standard AC.

equation, where the pseudo-first-order kinetic modeling should be linear with respect to the equation[35]

$$\ln[q_e - q(t)] = -k_1 t + \ln(q_e) \quad (1)$$

where $q(t)$ and q_e are the amount (in mg/g) of adsorbate adsorbed at any given time, t, and at equilibrium, respectively, and where k_1 is the rate constant for the pseudo-first-order kinetic model. Tran et al. also mention Blanchard et al., who initially proposed the second-order rate equation in 1984 for the removal of heavy metals in water and that the pseudo-second-order kinetic model should be linear with respect to the equation[36]

$$\frac{t}{q(t)} = \left(\frac{1}{q_e}\right)t + \frac{1}{k_2 q_e^2} \quad (2)$$

where $q(t)$ and q_e are the amount (in mg/g) of adsorbate adsorbed at any given time, t, and at equilibrium, respectively, and where k_2 is the rate constant for the pseudo-second-order kinetic model. Table 7 provides a summary of the kinetic modeling for each of the activated carbons used in this study.

Modeling of kinetic data provides information regarding the adsorption process of the reaction. The pseudo-first-order kinetic modeling assumes that one of the reactants or analytes is present in excess, while the pseudo-second-order kinetics assumes that the rate-limiting step in the reaction or adsorption is the chemical adsorption itself.[36,39] This would indicate that the adsorption rate is dependent on the adsorption capacity of the adsorbent rather than the concentration of the adsorbate.[37,38]

The commercial activated carbon clearly fits a pseudo-second-order model better than the pseudo-first-order model. This is clear by the linear correlation in the two models (0.9968 in pseudo-second-order vs 0.8550 in pseudo-first-order). This is also consistent with the q_e value obtained in the pseudo-second-order modeling of 8.61 mg/g, as the experimental q_e after 6 h was determined to be 8.46 ± 0.34 mg/g. This is significantly different in the pseudo-first-order model, where q_e is calculated as 2.91 mg/g.

The standard activated carbon fits both the pseudo-first- and pseudo-second-order kinetic models based on the linear correlation of the two models (0.9955 and 0.9967, respectively). The rate constants k_1 and k_2 are also very similar between the two different models (0.0135 and 0.0235, respectively). The biggest difference between the two models is the calculated q_e value. In the pseudo-first-order model, q_e is calculated to be 1.30 mg/g, while in the pseudo-second-order model, q_e is calculated to be 2.17 mg/g. The calculated q_e value from the pseudo-second-order kinetic model is closer to the experimental q_e obtained after 6 h of 2.08 ± 0.11 mg/g, indicating that the standard activated carbon also follows pseudo-second-order modeling.

Like the commercial activated carbon, the iron-loaded activated carbon very clearly follows the pseudo-second-order kinetic modeling. This is evident by the high linearity observed under second-order conditions (0.9980) compared to the significantly lower linearity observed in the pseudo-first-order modeling (0.9330). Similarly, the q_e value obtained using pseudo-first-order modeling of 1.75 mg/g is significantly lower than the experimental q_e obtained after 6 h of 4.86 ± 0.17 mg/g. The experimental q_e fits more with the pseudo-second-order modeling q_e of 4.95 mg/g.

Like the standard activated carbon, the manganese-loaded activated carbon fits both pseudo-first- and pseudo-second-order modeling based on the linear correlation of the kinetic models (0.9953 and 0.9948, respectively). The rate constants, however, are very different between the two models. The rate constant k_1, calculated for pseudo-first-order modeling, is much higher than the rate constant k_2, calculated for pseudo-second-order modeling. This indicates that the rate-determining conditions follow the conditions given by the pseudo-second-order modeling; in other words, the rate of the adsorption is dependent on the chemical adsorption itself. It is also evident that, while the Mn-loaded AC follows pseudo-first-order kinetic modeling with respect to linear correlation, the calculated q_e value from pseudo-first-order modeling is significantly different than the experiment q_e value obtained after 6 h (3.23 mg/g compared to 6.02 ± 0.16 mg/g, respectively). Pseudo-second-order modeling calculates q_e as 6.25 mg/g, which is much more closely related to the experimental q_e, indicating that pseudo-second-order modeling is more appropriate for kinetic modeling of the Mn-loaded AC.

Finally, the FeMn AC shows a very high linear correlation in the pseudo-second-order kinetic modeling (0.9951) and significantly lower correlation in the pseudo-first-order modeling (0.8416). This indicates that the FeMn AC fits pseudo-second-order modeling much better than pseudo-first-order modeling. This is consistent with the calculated q_e values from the two models, where q_e for the pseudo-first-order model is 4.63 mg/g and q_e for the pseudo-second-order model is 13.12 mg/g. The experimental q_e of 12.88 ± 0.58 mg/g after 6 h is much more consistent with the second-order kinetic modeling.

Based on the kinetic modeling of the activated carbons, all of the materials investigated in this study follow pseudo-second-order kinetics, indicating that the rate of adsorption is dependent

https://doi.org/10.1021/acsomega.3c02078
ACS Omega 2023, 8, 29083−29100

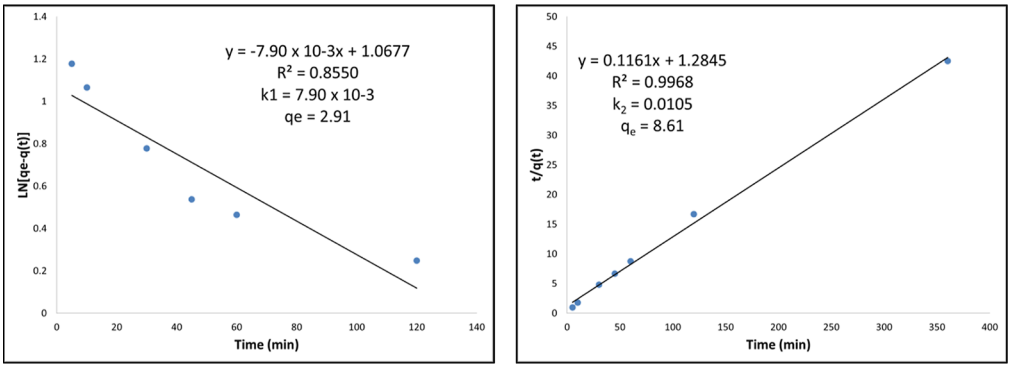

Figure D2. Pseudo-first (left) and pseudo-second (right) order kinetic models for the adsorption of As(V) using the commercial AC.

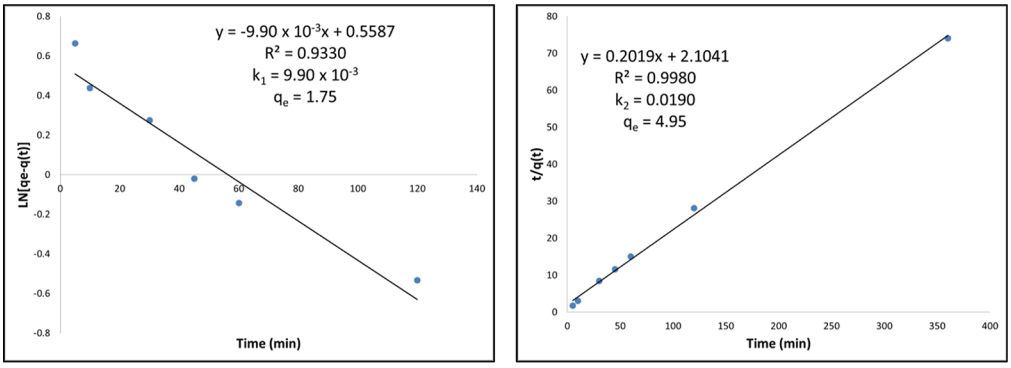

Figure D3. Pseudo-first (left) and pseudo-second (right) order kinetic models for the adsorption of As(V) using the Fe-loaded AC.

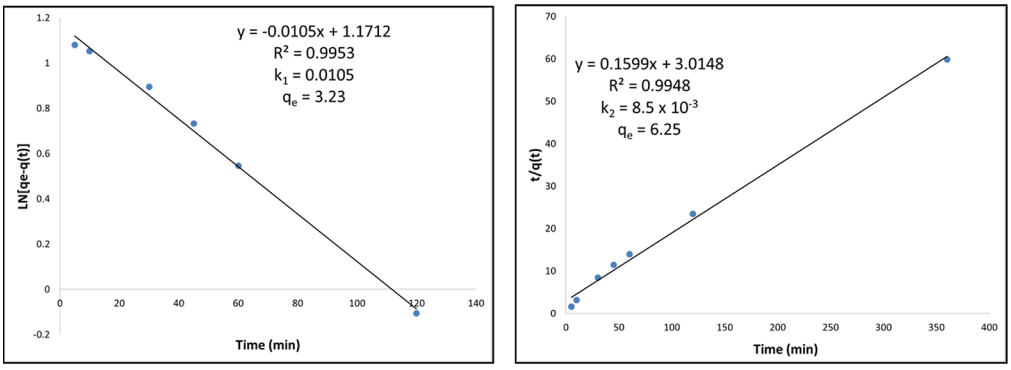

Figure D4. Pseudo-first (left) and pseudo-second (right) order kinetic models for the adsorption of As(V) using the Mn-loaded AC.

on the arsenic's adsorption onto the material, not on the concentration of the arsenic. Figure 11, below, provides an example of the pseudo-first- and pseudo-second-order kinetic modeling of the FeMn-loaded activated carbon. Appendix D, Figures D1−D2D3D4 show the pseudo-first- and pseudo-second-order kinetic models of the other activated carbon materials.

3.7.3. Arsenic(III) Kinetic Curves. To demonstrate that the FeMn-loaded AC was effective for arsenic(III) adsorption without the need for oxidation, adsorption kinetics of arsenic-(III) were obtained for the FeMn-loaded AC and compared to the arsenic(III) kinetics of the standard AC and commercial AC.

As expected, the maximum arsenic(III) adsorption was lower than the maximum arsenic(V) adsorption despite having a longer adsorption period. This is consistent with previous research in the literature stating arsenic(III) must generally be oxidized to arsenic(V) before removal, as adsorption is very efficient for the pentavalent arsenic species but not the trivalent arsenic species.[40] Once again, the metal-loaded activated carbon presented in this work outperforms the adsorption capacity of the standard activated carbon and the commercial benchmark, reaching 37.15 ± 2.04% total arsenic(III) adsorption (9.28 ± 0.61 mg/g) compared to the 15.09 ± 0.13% (3.59 ± 0.07 mg/g) and 12.81 ± 0.79% (2.92 ± 0.12 mg/g) observed in the standard and commercial activated carbons, respectively. Kinetics curves for arsenic(III) adsorption are given in Figure 12.

3.7.4. Arsenic(III) Kinetic Modeling. Kinetic modeling of the arsenic(III) kinetics curves was also done using the kinetic modeling described in Section 3.7.2. Table 8 provides a summary of the modeling for the adsorption of arsenic(III).

All three activated carbons investigated for arsenic(III) adsorption very clearly follow pseudo-second-order kinetic modeling. This is evident due to their strong linear correlation to the second-order modeling. This is also evident when comparing the calculated q_e values to the experimental q_e values for each activated carbon. For the commercial activated carbon,

https://doi.org/10.1021/acsomega.3c02078
ACS Omega 2023, 8, 29083−29100

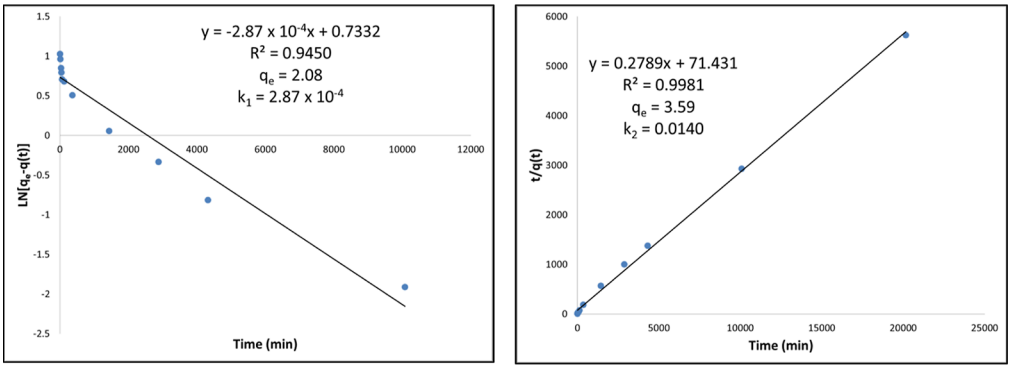

Figure E1. Pseudo-first (left) and pseudo-second (right) order kinetic models for the adsorption of As(III) using the standard AC.

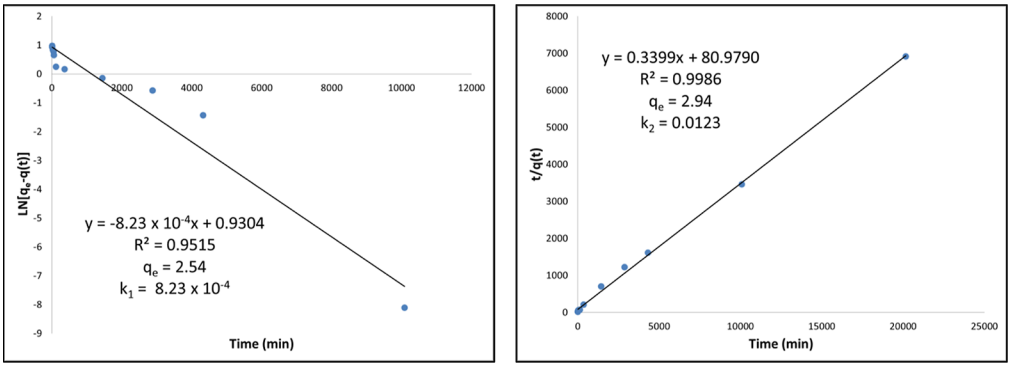

Figure E2. Pseudo-first (left) and pseudo-second (right) order kinetic models for the adsorption of As(III) using the commercial AC.

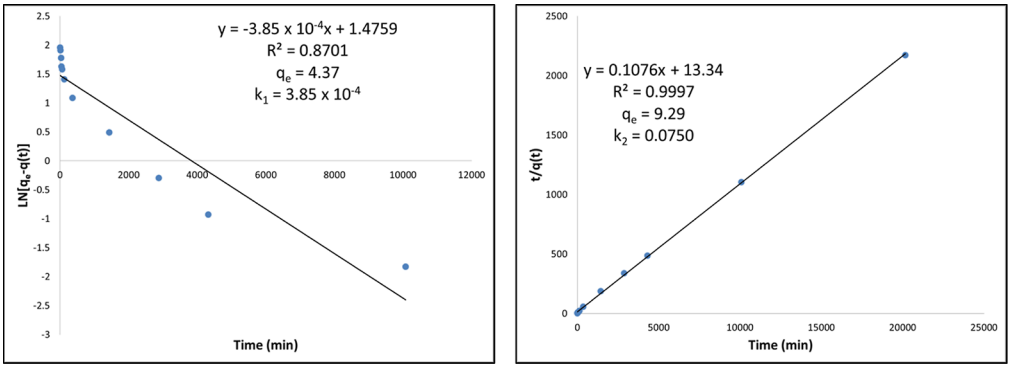

Figure E3. Pseudo-first (left) and pseudo-second (right) order kinetic models for the adsorption of As(III) using the FeMn-loaded AC.

experimental q_e was 2.92 ± 0.12 mg/g, for the standard AC, 3.59 ± 0.43 mg/g, and for the FeMn AC, 9.28 ± 0.61 mg/g. When comparing these to the modeling q_e values, there is a significant difference observed between the pseudo-first-order q_e values and the experimental values, while no significant difference is observed between the experimental q_e and the pseudo-second-order model q_e values. This implies that the rate-limiting factor is the arsenic(III) adsorption onto the activated carbon itself, rather than the adsorbate or adsorbent being present in excess. Kinetic modeling of the activated carbons for arsenic(III) adsorption kinetics is provided in Appendix E, Figures E1−E3.

3.8. Literature Comparison. As indicated in Table 9, many studies have been done to investigate the adsorption of arsenic by various adsorbent materials. While the activated carbon materials presented in this study outperform some adsorbents outlined in the literature, it is outperformed by others. Despite being outperformed by some adsorbent materials presented in the literature, this activated carbon is a cost-effective and efficient means of removing arsenic from acidic waters. The abundance of the feedstock and the high carbon content in the raw feedstock allow for the adsorbent to be produced with little cost associated and resources allocated to the preparation of the material. In addition, intentionally low amounts of KOH are used to activate the material, with parallel studies investigating the potential for KOH recycling to further increase the cost-effectiveness of the material.

4. CONCLUSIONS

An efficient activated carbon produced using minimal KOH activating agent and a readily available petcoke feedstock was used for arsenic(V) and arsenic(III) adsorption using metal-doped activated carbons. Metal loading of the activated carbons resulted in a significant increase in the adsorption capacity for arsenic, surpassing that of the benchmark commercial activated carbon. Adsorption capacity comparisons normalized to surface

https://doi.org/10.1021/acsomega.3c02078
ACS Omega 2023, 8, 29083−29100

area and microporosity indicate that the functionality of the activated carbon's surface is a more crucial factor in adsorption than high surface area or extensive microporosity. The adsorption of arsenic in the binary-FeMn-loaded activated carbon far exceeded that of the other activated carbons investigated. XPS of the activated carbons showed significant changes in the speciation of the iron and manganese present on the activated carbon post-arsenic exposure, leading to the conclusion that arsenic is being physisorbed to the metal-loaded surface through redox reactions. The PC-activated carbon produced using this method is effective in the adsorption of arsenic species in solution and is a cost-effective method for the removal of arsenic contamination in waters using excess PC.

APPENDIX A

APPENDIX B

APPENDIX C

APPENDIX D

APPENDIX E

AUTHOR INFORMATION

Corresponding Author

Andrew J. Vreugdenhil − *Materials Science Graduate Program, Trent University, Peterborough, Ontario K9L 0G2, Canada; Department of Chemistry, Trent University, Peterborough, Ontario K9L 0G2, Canada;* orcid.org/0000-0002-1197-2847; Phone: +1-(705)-748-1011; Email: avreugdenhil@trentu.ca

Author

Kyle S. Fisher − *Materials Science Graduate Program, Trent University, Peterborough, Ontario K9L 0G2, Canada*

Complete contact information is available at: https://pubs.acs.org/10.1021/acsomega.3c02078

Author Contributions

Conceptualization, K.S.F., A.J.V.; methodology, K.S.F.; formal analysis, K.S.F.; investigation, K.S.F.; resources, A.J.V.; writing—original draft, K.S.F.; writing—review and editing, A.J.V.; supervision, A.J.V.; and funding acquisition, A.J.V. All authors have read and agreed to the published version of the manuscript.

Notes

The authors declare no competing financial interest.

ACKNOWLEDGMENTS

Acknowledgements to Oliver Strong and Kevin Scotland for their assistance in proofreading the manuscript and for all their input during this process. Also, our thanks to the Trent University IMRL laboratory group for their support and interest.

REFERENCES

(1) National Research Council. *Arsenic: Medical and Biological Effects of Environmental Pollutants*; National Academy of Sciences, 1977.

(2) de Andrade, R. P.; Santana Filho, S.; Mello, J. W. V. d.; Figueiredo, B. R. d.; Dussin, T. M.; Dussin, T. . M. Arsenic mobilization from sulfidic materials from gold mines in Minas Gerais State. *Quim. Nova* **2008**, *31*, 1127−1130.

(3) Clark, I. D.; Raven, K. G. Sources and Circulation of Water and Arsenic in the Giant Mine, Yellowknife, NWT, Canada. *Isot. Environ. Health Stud.* **2004**, *40*, 115.

(4) Society for Mining, Metallurgy, and Exploration. The Role of Arsenic in the Mining Industry. April 2015, Available Online: https://me.smenet.org/docs/Publications/ME/Issue/TheRoleofArsenicintheMiningIndustry.pdf (accessed 2 June 2023).

(5) World Health Organization. Arsenic. Feb. 15, 2018, Available Online: https://www.who.int/news-room/fact-sheets/detail/arsenic#:~:text=Arsenic%20is%20highly%20toxic%20in,cause%20cancer%20and%20skin%20lesions (accessed 2 June 2023).

(6) World Health Organization. Drinking Water. March 21, 2022, Available Online: https://www.who.int/news-room/fact-sheets/detail/drinking-water (accessed 2 June 2023).

(7) Khulbe, K. C.; Matsuura, T. Removal of heavy metals and pollutants by membrane adsorption techniques. *Appl. Water Sci.* **2018**, *8*, 19.

(8) Gomase, V.; Jugade, R.; Doondani, P.; Saravanan, D.; Pandey, S. Sequential modifications of chitosan biopolymer for enhanced confiscation of Cr (VI). *Inorg. Chem. Commun.* **2022**, *145*, 110009.

(9) Byambaa, E.; Seon, J.; Kim, T. H.; Kim, S. D.; Ji, W. H.; Hwang, Y. Arsenic (V) Removal by an Adsorbent Material Derived from Acid Mine Drainage Sludge. *Appl. Sci.* **2020**, *11*, 47.

(10) Singh, S.; Naik, T. S. S. K.; U, B.; Khan, N. A.; Wani, A. B.; Behera, S. K.; Nath, B.; Bhati, S.; Singh, J.; Ramamurthy, P. C. A systematic study of arsenic adsorption and removal from aqueous environments using novel graphene oxide functionalized UiO-66NDC nanocomposites. *Sci. Rep.* **2022**, *12*, 15802.

(11) Rahdar, S.; Taghavi, M.; Khaksefidi, R.; Ahmadi, S. Adsorption of arsenic (V) from aqueous solution using modified saxaul ash: isotherm and thermodynamic study. *Appl. Wat. Sci.* **2019**, *9*, 87.

(12) Liu, C.-H.; Chuang, Y. H.; Chen, T. Y.; Tian, Y.; Li, H.; Wang, M. K.; Zhang, W. Mechanism of Arsenic Adsorption on Magnetite Nanoparticles from Water: Thermodynamic and Spectroscopic Studies. *Environ. Sci. Technol.* **2015**, *49*, 7726−7734.

(13) Zhang, J.; Ding, T.; Zhang, Z.; Xu, L.; Zhang, C. Enhanced Adsorption of Trivalent Arsenic from Water by Functionalized Diatom Silica Shells. *PLoS One* **2015**, *10*, No. e0123395.

(14) Yao, S.; Liu, Z.; Shi, Z. Arsenic removal from aqueous solutions by adsorption onto iron oxide/activated carbon magnetic composite. *J. Environ. Health Sci. Eng.* **2014**, *12*, 58.

(15) Pourrezaei, P.; Alpatova, A.; Khosravi, K.; Drzewicz, P.; Chen, Y.; Chelme-Ayala, P.; Gamal El-Din, M. Removal of organic compounds and trace metals from oil sands process-affected water using zero valent iron enhanced by petroleum coke. *J. Environ. Manage.* **2014**, *139*, 50−58.

(16) Karimi, A.; Thinon, O.; Fournier, J.; Hill, J. M. Activated Carbon Prepared from Canadian Oil Sands Coke by CO_2 Activation: II. Adsorption of Metallic Ions and Organic Constituents from Oil Sands Tailings Water. *Can. J. Chem. Eng.* **2013**, *91*, 1500−1507.

(17) Mondal, M. K.; Garg, R. A Comprehensive Review on Removal of Arsenic using Activated Carbon Prepared from Easily Available Waste Materials. *Environ. Sci. Pollut. Res.* **2017**, *24*, 13295−13306.

(18) OilChange International. Petroleum Coke: The Coal Hiding in the Tar Sands Report. Jan. 2013, Available Online: https://priceofoil.org/content/uploads/2013/01/OCI.Petcoke.FINALSCREEN.pdf (accessed 2 June 2023).

(19) Tadda, M. A.; Ahsan, A.; Shitu, A.; ElSergany, M.; Arunkumar, T.; Jose, B.; Razzaque, M. A.; Daud, N. N. N. A review on activated carbon: process, application and prospects. *J. Adv. Civ. Environ. Eng. Pract. Res.* **2016**, *2*, 7−13.

(20) Celzard, A.; Fierro, V.; Marêché, J. F.; Furdin, G. Advanced Preparative Strategies for Activated Carbons Designed for the Adsorptive Storage of Hydrogen. *Adsorb. Sci. Technol.* **2007**, *25*, 129−142.

(21) Rouzaud, J. N.; Oberlin, A. Structure, microtexture, and optical properties of anthracene and saccharose-based carbons. *Carbon* **1989**, *27*, 517−529.

https://doi.org/10.1021/acsomega.3c02078
ACS Omega 2023, 8, 29083−29100

(22) Kuraray Co. LTD. Raw Materials, Available Online: http://www.kuraray-c.co.jp/en/activecarbon/about/03.html (accessed 2 June 2023).
(23) Agico Cement. Carbonization, Available Online: https://agicokiln.com/activated-carbon-production-line/?gclid=Cj0KCQiA54KfBhCKARIsAJzSrdoZEBh5CB25XivRVl7odjU-N1ou3_aLmokTKj5S7i7oDZue8BBejEsaAsZaEALw_wcB (accessed 2 June 2023).
(24) Fisher, K. S.; Vreugdenhil, A. J. Adsorption of Chromium (VI) Using an Activated Carbon Derived from Petroleum Coke Feedstock. *Int. J. Mol. Sci.* **2022**, *23*, 16172.
(25) Strong, O. K. L.; Nazari, E.; Roy, T.; Scotland, K. M.; Pede, P. R.; Vreugdenhil, A. J. Transforming micropores to mesopores by heat cycling KOH activated petcoke for improved kinetics of adsorption of naphthenic acids. *Heliyon* **2023**, *9*, No. e13500.
(26) Nesbitt, H. W.; Banerjee, D. Interpretation of XPS Mn(2p) spectra of Mn oxyhydroxides and constraints on the mechanism of MnO_2 precipitation. *Am. Min.* **1998**, *83*, 305−315.
(27) Grosvenor, A. P.; Kobe, B. A.; Biesinger, M. C.; McIntyre, N. S. Investigation of multiplet splitting of Fe 2p XPS spectra and bonding in iron compounds. *Surf. Interface Anal.* **2004**, *36*, 1564−1574.
(28) Surface Science Western. X-Ray Photoelectron Spectroscopy (XPS) Reference Pages. Multiplet Splitting, Available Online: http://www.xpsfitting.com/2008/09/multiplet-splitting.html (accessed 2 June 2023).
(29) Surface Science Western. X-Ray Photoelectron Spectroscopy (XPS) Reference Pages. Arsenic, Available Online: http://www.xpsfitting.com/search/label/Arsenic (accessed 2 June 2023).
(30) Surface Science Western. X-Ray Photoelectron Spectroscopy (XPS) Reference Pages. Iron, Available Online: http://www.xpsfitting.com/search/label/Iron (accessed 2 June 2023).
(31) Surface Science Western. X-Ray Photoelectron Spectroscopy (XPS) Reference Pages. Manganese, Available Online: http://www.xpsfitting.com/search/label/Manganese (accessed 2 June 2023).
(32) Naumkin, A. V.; Kraut-Vass, A.; Gaarenstroom, S. W.; Powel, C. J. NIST X-ray Photoelectron Spectroscopy Database. 2012, Available Online: https://srdata.nist.gov/xps/ (accessed 2 June 2023).
(33) Surface Science Western. X-ray Photoelectron Spectroscopy (XPS) Reference Pages. Oxygen, Available online: http://www.xpsfitting.com/search/label/Oxygen (accessed 2 June 2023).
(34) Rahman, M. M.; Hafez, I.; Tajvidi, M.; Amirbahman, A. Highly Efficient Iron Oxide Nanoparticles Immobilized on Cellulose Nanofibril Aerogels for Arsenic Removal from Water. *Nanomaterials* **2021**, *11*, 2818.
(35) Chiavola, A.; D'Amato, E.; Stoller, M.; Chianese, A.; Boni, M. R. Application of Iron Based Nanoparticles as Adsorbents for Arsenic Removal from Water. *Chem. Eng. Trans.* **2016**, *47*, 325.
(36) Tran, H. N.; You, S.-J.; Hosseini-Bandegharaei, A.; Chao, H. P.; Chao, H.-P. Mistakes and inconsistencies regarding adsorption of contaminants from aqueous solutions: A critical review. *Water Res.* **2017**, *120*, 88−116.
(37) Lagergren, S. About the theory of so-called adsorption of soluble substances. *K. Sven. Vetensk. Handl.* **1898**, *24*, 1−39. ; in press
(38) Blanchard, G.; Maunaye, M.; Martin, G. Removal of heavy metals from waters by means of natural zeolites. *Water Res.* **1984**, *18*, 1501−1507.
(39) Revellame, E. D.; Fortela, D. L.; Sharp, W.; Hernandez, R.; Zappi, M. E. Adsorption kinetic modeling using pseudo-first order and pseudo-second order rate laws: A review. *Clean. Eng. Technol.* **2020**, *1*, 100032.
(40) Tolkou, A. K.; Kyzas, G. Z.; Katsoyiannis, I. A. Arsenic (III) and Arsenic (V) Removal from Water Sources by Molecularly Imprinted Polymers (MIPs): A Mini Review of Recent Developments. *Sustainability* **2022**, *14*, 5222.
(41) Shakoor, M. B.; Niazi, N. K.; Bibi, I.; Shahid, M.; Saqib, Z. A.; Nawaz, M. F.; Shaheen, S. M.; Wang, H.; Tsang, D. C.; Bundschuh, J.; et al. Exploring the arsenic removal potential of various biosorbents from water. *Environ. Int.* **2019**, *123*, 567−579.

https://doi.org/10.1021/acsomega.3c02078
ACS Omega 2023, 8, 29083−29100